ADVANCED ENERGY MATERIALS

Supporting Information

for *Adv. Energy Mater.,* DOI: 10.1002/aenm.202103368

Single-Atom Reversible Lithiophilic Sites toward Stable Lithium Anodes

Zhilin Yang, Yan Dang, Pengbo Zhai, Yi Wei, Qian Chen, Jinghan Zuo, Xiaokang Gu, Yong Yao, Xingguo Wang, Feifei Zhao, Jinliang Wang, Shubin Yang, Peizhe Tang, and Yongji Gong**

WILEY-VCH

Supporting Information

Single-Atom Reversible Lithiophilic Sites towards Stable Lithium Anodes

Zhilin Yang, Yan Dang, Pengbo Zhai, Yi Wei, Qian Chen, Jinghan Zuo, Xiaokang Gu, Yong Yao, Xingguo Wang, Feifei Zhao, Jinliang Wang, Shubin Yang, Peizhe Tang and Yongji Gong**

Z. Yang, Y. Dang, Q. Chen, J. Zuo, X. Gu, Y. Yao, X. Wang, Dr. F. Zhao, Prof. S. Yang, Prof. P. Tang, Prof. Y. Gong
School of Materials Science and Engineering
Beihang University
Beijing 100191, China
E-mail: Peizhet@buaa.edu.cn; yongjigong@buaa.edu.cn

Z. Yang, Prof. J. Wang
School of Physics
Beihang University
Beijing 100191, China

Dr. P. Zhai
College of Physics
Qingdao University
Qingdao 266071, China

Y. Wei
Beijing Key Laboratory of Electrochemical Process and Technology for Materials
Beijing University of Chemical Technology
Beijing 100029, China

Prof. P. Tang
Center for Free-Electron Laser Science
Max Planck Institute for the Structure and Dynamics of Matter
Hamburg 22761, Germany

Prof. Y. Gong
Center for Micro-Nano Innovation
Beihang University
Beijing 100191, China

Materials and Reagents

All reagents and solvents were purchased from Alfa Aesar or Aladdin and used as received without further purification. The $LiFePO_4$ (LFP) cathode material and Li foils were supplied by MTI Corporation.

Preparation of the SA*M*@NG (*M* = Mn, Ni, Co, Zn, Cu, Zr) Materials

SA*M*@NG (*M*=Mn, Ni, Co, Zn, Cu, Zr) were synthesized through a facile salt-templating strategy. Typically, 8.5g, 0.62 g, 1.2 g and 32.12 mg of NaCl, glucose($C_6H_{12}O_6$), dicyanamide ($C_2H_4N_4$) and manganese acetate tetrahydrate (Mn $(CH_3COO)_2 \cdot 4H_2O$) were added to deionized water (75 mL) by magnetic stirring to ensure a homogeneous solution, respectively. The solution was immediately frozen under -50 ℃ and freeze-dried in a freeze dryer under vacuum at the sublimating temperature of -48 °C for 48 h. Then, the resulting white powder was transferred into a quartz boat. After that, the boat was held in a tube furnace and ramped at a rate of 4 °C/min before reaching at 760 °C under Ar (80 sccm) atmosphere. The reaction duration is 2 h before cooling down to room temperature naturally. The black powder was dispersed into deionized water to dissolve the template. Subsequently, the SAMn@NG sample was obtained after being filtrated, washed several times with deionized water, and dried in a vacuum at 60 °C overnight. Before achieving the final products, the samples were annealed for the second time at 900 ℃ for 1 h with a heating rate of 5 ℃/min under Ar (80 sccm) atmosphere. Similarly, SANi@NG, SACo@NG, SAZn@NG, SACu@NG and SAZr@NG were prepared.

Preparation of the NG and G Materials

The control sample of NG was prepared under the same preparation condition except that the metal salt was not added into the precursor solution. And the frication process of G was similar to that of the NG except that the dicyanamide was not added into the precursor solution.

Electrochemical Measurements

CR2025-type coin cells were assembled to deposit Li on the different electrode material (Li foil as both counter and reference electrode) to evaluate the battery cycling performance by galvanostatic experiments. The separator (Celgard 2400) was used to separate the Li foil and the working electrode. All the coin cells were assembled in an Ar-filled glove box with O_2 and H_2O content < 0.1 ppm. 50 μl electrolyte of 1.0 M lithium bis (trifluoromethane sulfonimide) (LiTFSI) in 1,3-dioxolane (DOL)/1,2-dimethoxyethane (DME) (1:1 by volume) with 2 wt% $LiNO_3$ additives was used in assembling cell for investigating the Li plating/stripping process and measuring the coulombic efficiency (CE). The CE of Li plating/stripping was calculated based on the ratio of Li capacity removed from the working electrode to that deposited during the same cycle. Active material and polyvinylidene difluoride (PVDF) were stirred in N-methyl pyrrolidone (NMP) for 3 h with a mass ratio of 4:1 to form a uniform slurry, which was then coated on a Cu foil through doctor blading. The final electrodes were obtained by drying in a vacuum oven at 85 ℃ overnight. All coin cells were tested in Neware BTS 4000 multichannel battery tester. Before test, each cell was first cycled at 0.01 - 1 V (vs Li/Li^+) at 0.05 mA cm^{-2} for five cycles to stabilize electrodes. Then, cycling tests were performed by depositing different capacities of Li (1.0, 2.0, 3.0, 5.0 mAh cm^{-2}) at different current densities (0.5, 1.0, 2.0 mA cm^{-2}) on the working electrodes, followed by Li stripping up to 1.0 V.

Full cell assembly

$LiFePO_4$ (LFP) cathodes with fixed areal capacities of 0.58 mAh cm^{-2} (3.4 mg cm^{-2}) were prepared by mixing LFP powders, Super C carbon black and PVDF with mass ratio of 8:1:1 in NMP. The resulted slurry was coated onto Al foil. Li-SAMn@NG, Li-SAZr@NG and Li-G anodes were obtained from preprocessed half cells, that is 0.6 mAh cm^{-2} of Li was

electrodeposited onto the SAMn@NG, SAZr@NG and G electrodes to obtain Li-SAMn@NG, Li-SAZr@NG and Li-G anodes in the coin cells by using Li foil as the reference and counter electrodes (N/P ratio ≈ 1), respectively. Then the anodes were extracted from the half cells and reassembled into full cells against 0.58 mAh cm^{-2} LFP cathode. All the full cells were cycled within the voltage range of 2.3 to 3.9 V (vs. Li/Li^+). Before assembling into a full battery, all LFP cathodes were first cycled five times paired with Li foils to stabilize the cathode electrolyte interphase (CEI).

Materials characterization

The crystal structure and morphology of the samples were examined by X-ray diffraction (XRD, Bruker AXS D8 Advance) with Cu Kα radiation (λ = 1.5406 Å), field-emission scanning electron microscopy (FESEM, Hitachi SU8020), and transmission electron microscopy (TEM, JEOL JEMF200). The chemical composition and elemental states were analyzed by X-ray photoelectron spectroscopy (XPS) on the ESCALAB 250Xi, (Thermo Fisher Scientific Inc., USA). High-angle annular dark-field scanning transmission electron microscopy (HAADF-STEM) characterization was conducted on a JEOL ARM200F equipped with a spherical aberration corrector under the accelerating voltage of 80 kV.

Computational Details

The first-principle electronic structure calculations were performed using density functional theory (DFT) as implemented in the Vienna Ab initio Simulation Package (VASP), and the calculation results were visualized in VESTA. [1-4] Generalized gradient approximation proposed by Perdew, Burke, and Ernzerhof was employed to understand the electron correlation. [5] The Gaussian smearing method was used and the width of smearing was chosen as 0.05 eV. [6] The energy cutoff for plane-wave expansion of the projector augmented waves (PAWs) was 550 eV. [7] All structures were fully optimized until the energy and residual force converge to 10^{-5} eV and 0.02eV $Å^{-1}$, respectively. The Vander Waals (vdW) corrections were considered to estimate accurately the strength of Li adsorption on SA*M*@NG

host. Dispersion energy correction of vdW interactions was incorporated by the semiempirical correction scheme of the Grimme (DFT-D3) method. [8, 9]

To simulate the interaction between Li and SA*M*@NG, a single-layered 6 × 6 × 1 graphene with *M*–N_4–C structure was constructed. Besides, a pyridinic nitrogen-doped graphene (NG) model (6 × 6 × 1) and graphene (G) model (6 × 6 × 1) was constructed as a comparison. The optimized lattice constant for the monolayer graphene was 2.468Å, which is slightly larger than the experimental value 2.46 Å.[10] The dipole corrections for potential and total energy were considered in this work. In the vertical direction, a vacuum layer of 25 Å was introduced for all the surfaces to avert artificial interactions between the periodically repeated images. The Brillouin zone (BZ)was sampled using the Monkhorst-Pack k-point mesh of 5 × 5 × 1 in the Gamma-centered grids for all the calculations.[11] The stable geometry structure and binding energy were obtained after the positions of all the atoms have been relaxed fully.

The binding energy of Li atoms was defined as $E_b = (E_{total} - E_{sub} - nE_{Li})/n$, where E_{sub} is the energy of the bare SA*M*@NG sheet (without any adatoms), E_{total} is the energy of the corresponding system with Li atom adsorbed, and E_{Li} is the energy of one isolated Li atom, n is the number of Li atoms adsorbed. The formula of binding energy indicates a negative value for successful adsorption, with a larger (more negative value) signifying stronger binding.

To study the adatom concentration effects on the binding energies of the systems, we chose the 4 × 4 × 1, 5 × 5 × 1, 6 × 6 × 1, 7 × 7 × 1, 8 × 8 × 1, 9 × 9 × 1, 10 × 10 × 1 and 11 × 11 × 1 supercell models with k-point meshes of 7 × 7 × 1, 6 × 6 × 1, 5 × 5 × 1, 4 × 4 × 1, 4 × 4 ×1, 3 × 3 × 1, 3 × 3 × 1and 3 × 3 × 1, respectively, for simulating changes in lithium concentrations. Lithium concentration X is defined as the number of Li occupied per unit base area, that is, X=1/S, where S is the supercell area used.

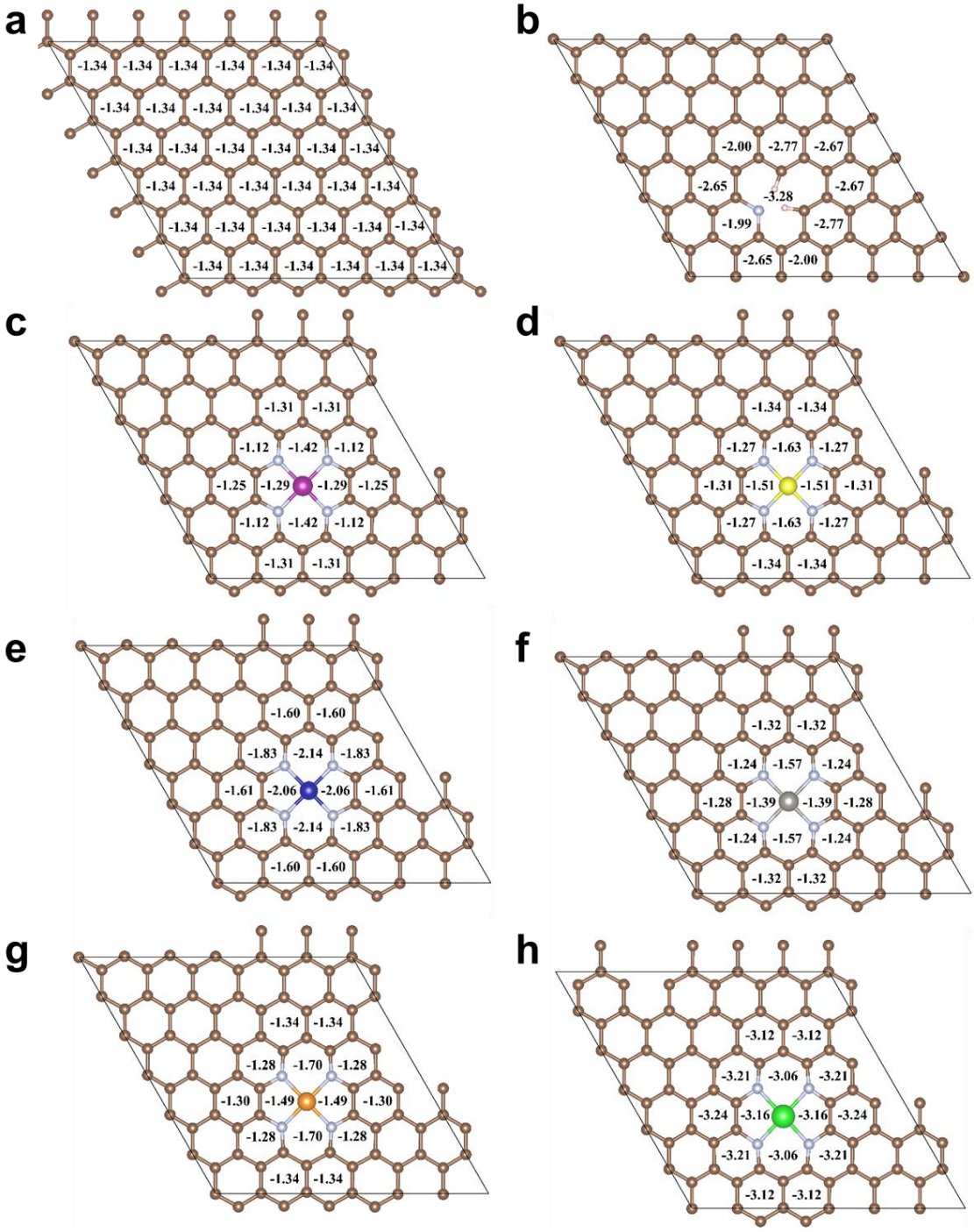

Figure S1. Li binding energy (eV/ Li-atom) mappings. (a) G, (b) NG, (c) SAMn@NG, (d) SANi@NG, (e) SACo@NG, (f) SAZn@NG, (g) SACu@NG and (h) SAZr@NG, respectively. The numbers indicate the binding energy of a Li atom at the corresponding positions of substrate. The carbon, nitrogen, manganese, nickel, cobalt, zinc, copper and

zirconium are marked with brown, silver, purple, yellow, dark blue, gray, orange and green, respectively.

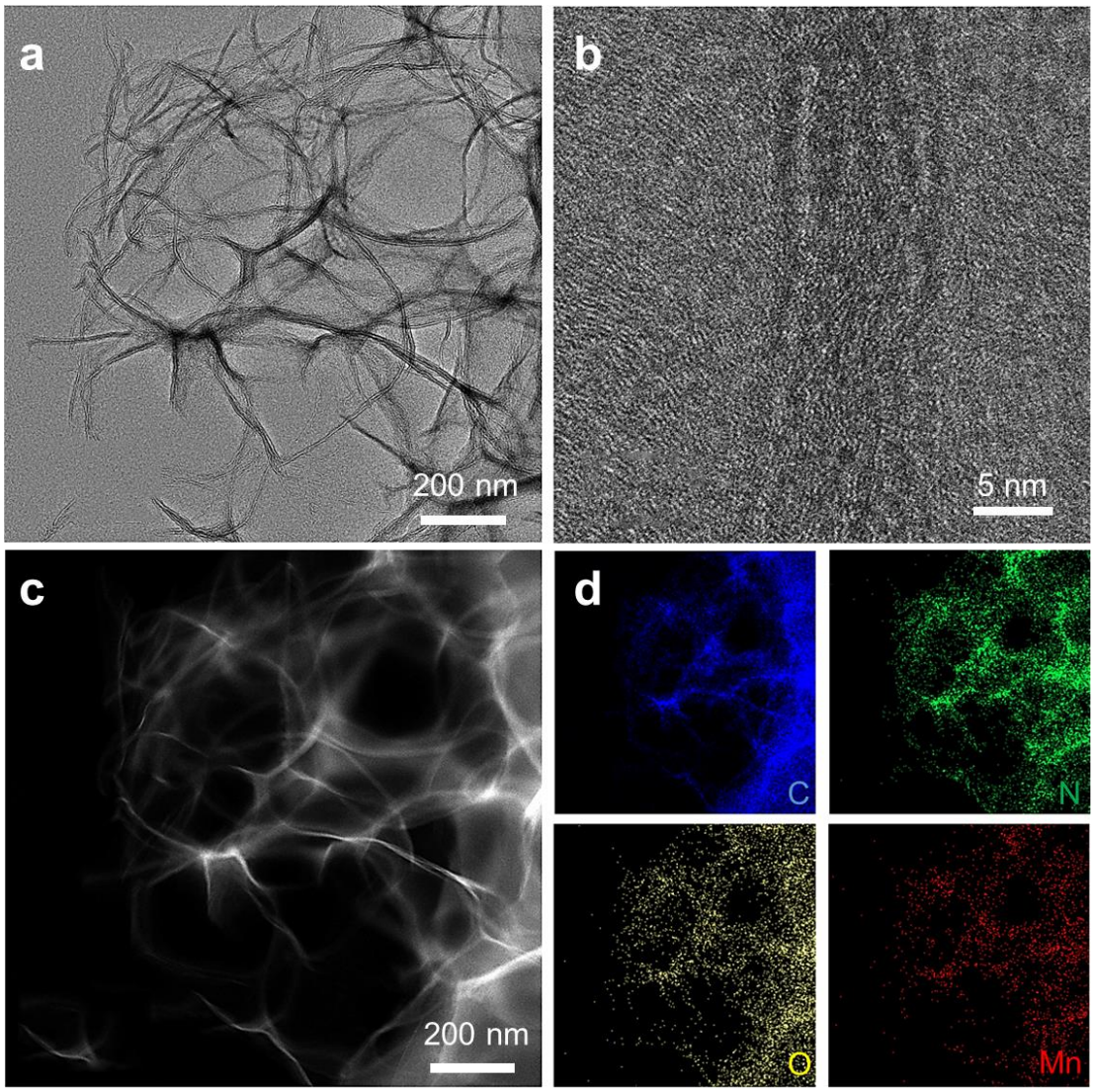

Figure S2. Characterization of the SAMn@NG based on TEM mode. (a) TEM image, (b) HRTEM image, (d) Elemental mapping of C, N, O and Mn based on the STEM image (c).

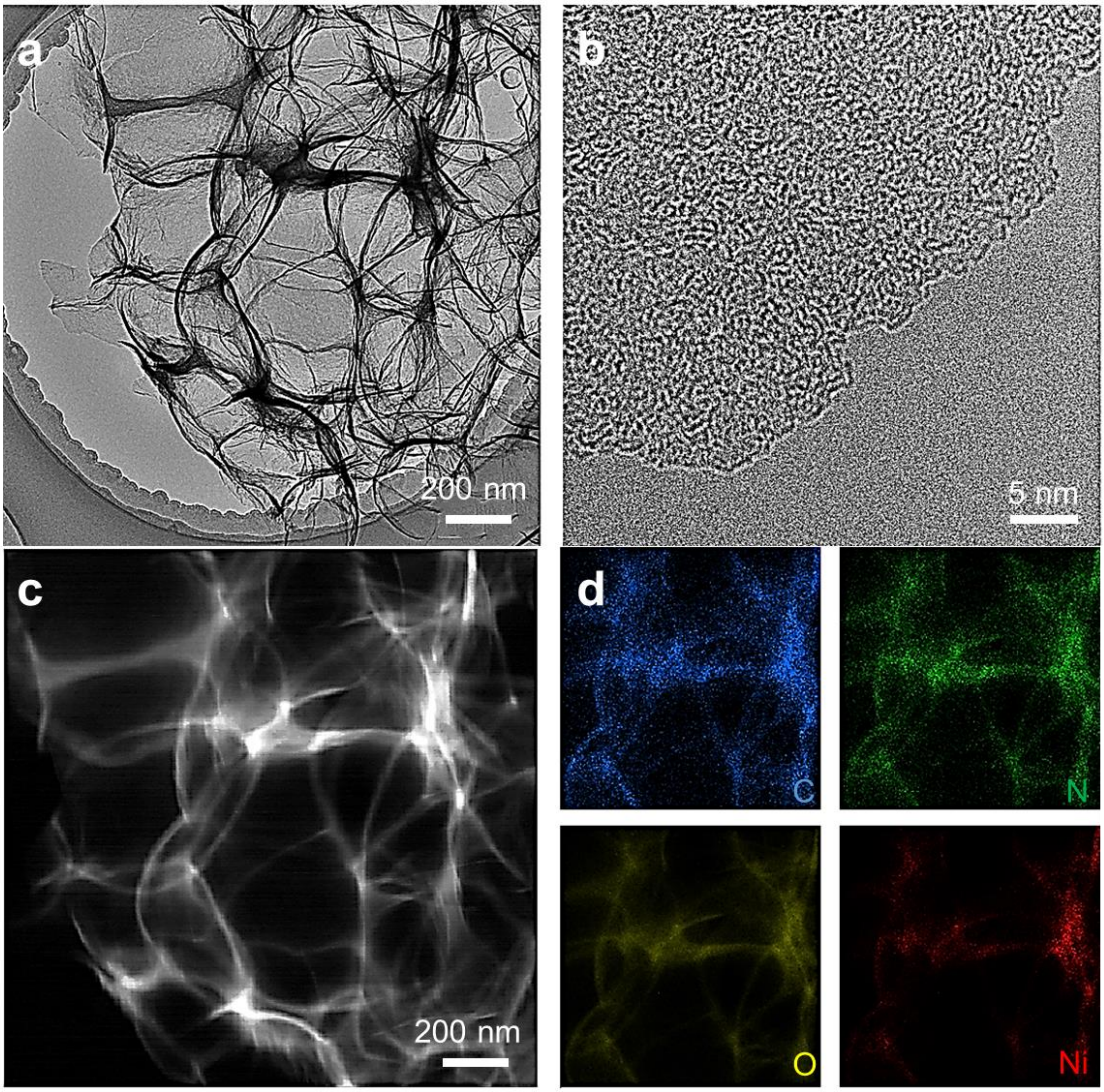

Figure S3. Characterization of the SANi@NG based on TEM mode. (a) TEM image, (b) HRTEM image, d) Elemental mapping of C, N, O and Ni based on the STEM image (c).

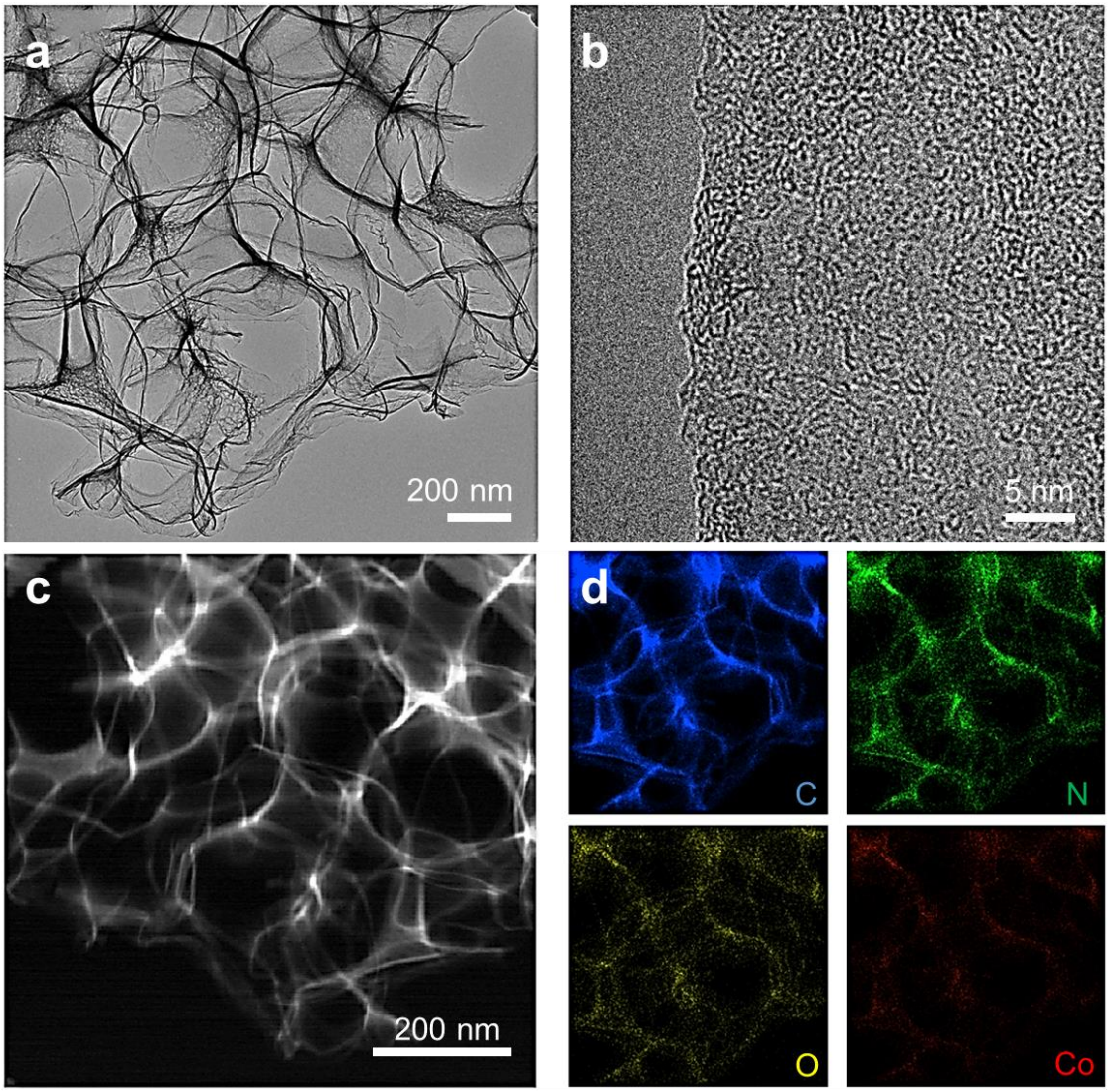

Figure S4. Characterization of the SACo@NG based on TEM mode. (a) TEM image, (b) HRTEM image, (d) Elemental mapping of C, N, O and Co based on the STEM image (c).

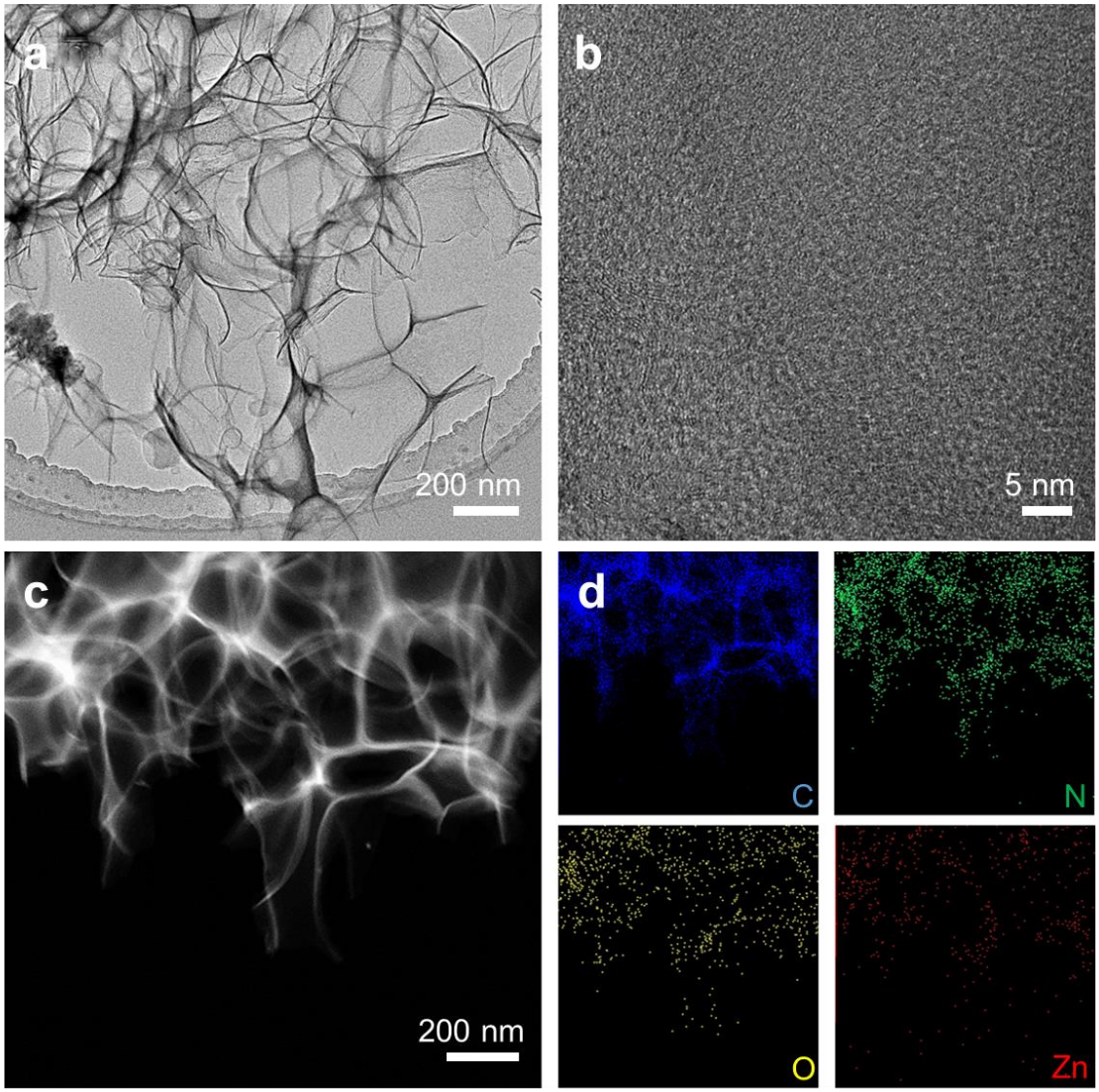

Figure S5. Characterization of the SAZn@NG based on TEM mode. (a) TEM image, (b) HRTEM image, (d) Elemental mapping of C, N, O and Zn based on the STEM image (c).

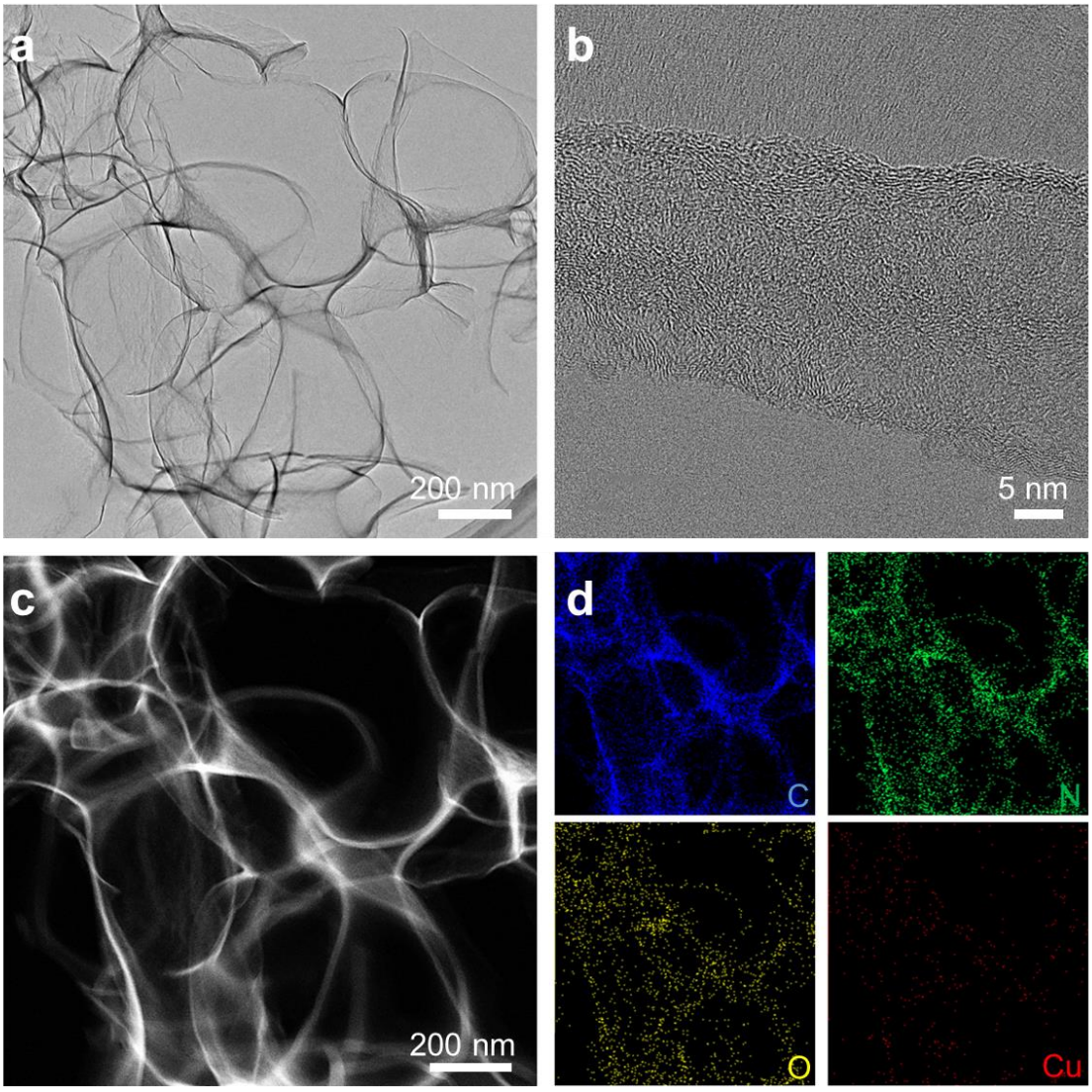

Figure S6. Characterization of the SACu@NG based on TEM mode. (a) TEM image, (b) HRTEM image, (d) Elemental mapping of C, N, O and Cu based on the STEM image (c).

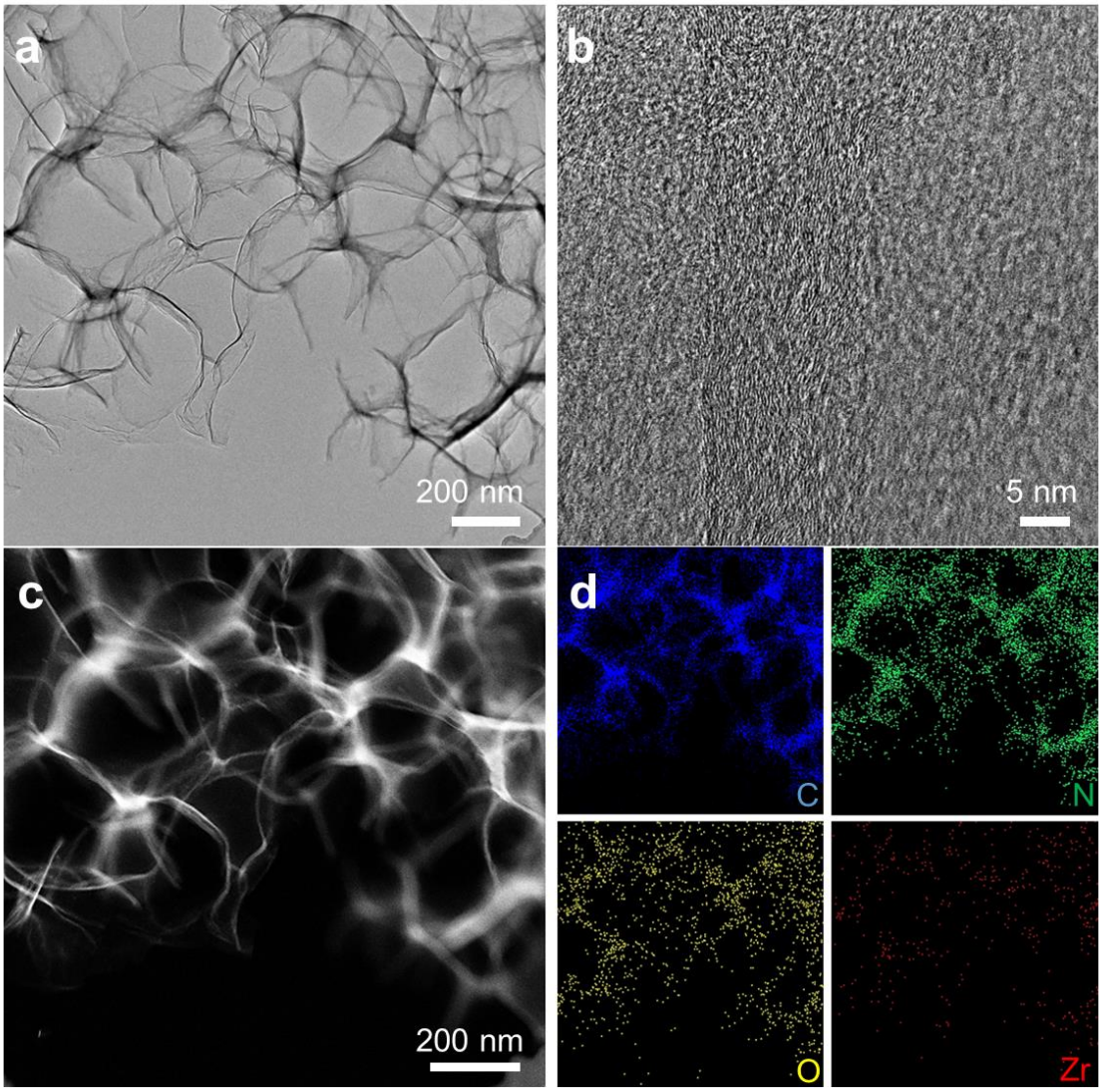

Figure S7. Characterization of the SAZr@NG based on TEM mode. (a) TEM image, (b) HRTEM image, (d) Elemental mapping of C, N, O and Zr based on the STEM image (c).

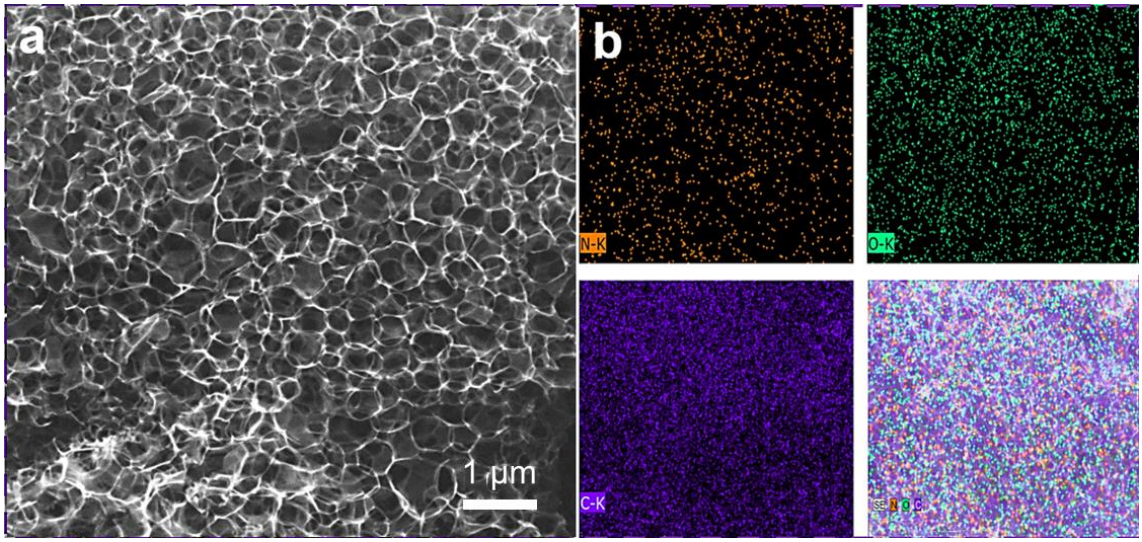

Figure S8. Characterization of the NG based on SEM mode. (a) SEM image, and corresponding (b) elemental mapping of C, N and O.

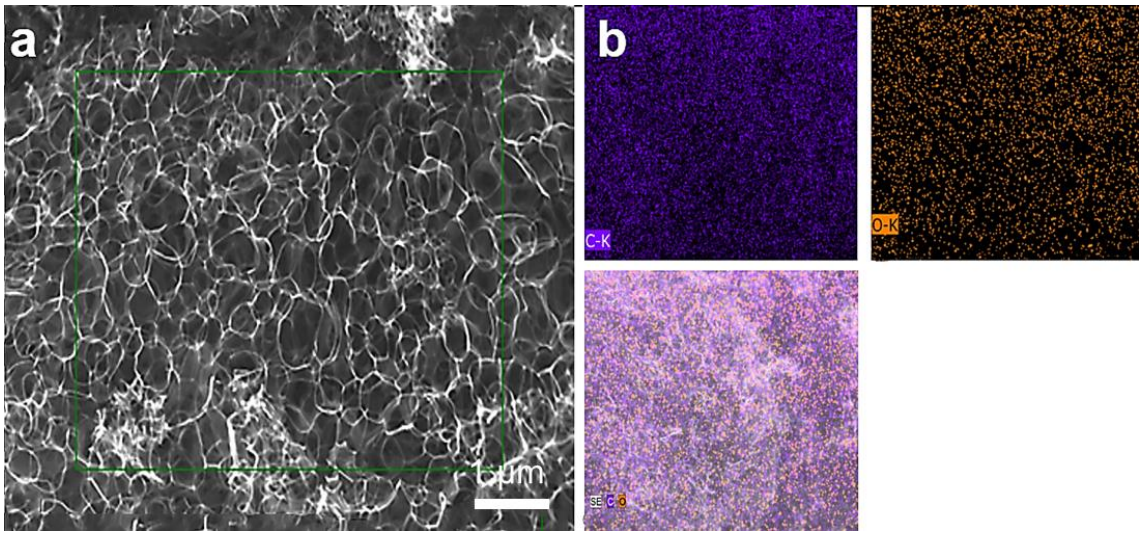

Figure S9. Characterization of the G based on SEM mode. (a) SEM image, and corresponding (b) elemental mapping of C and O.

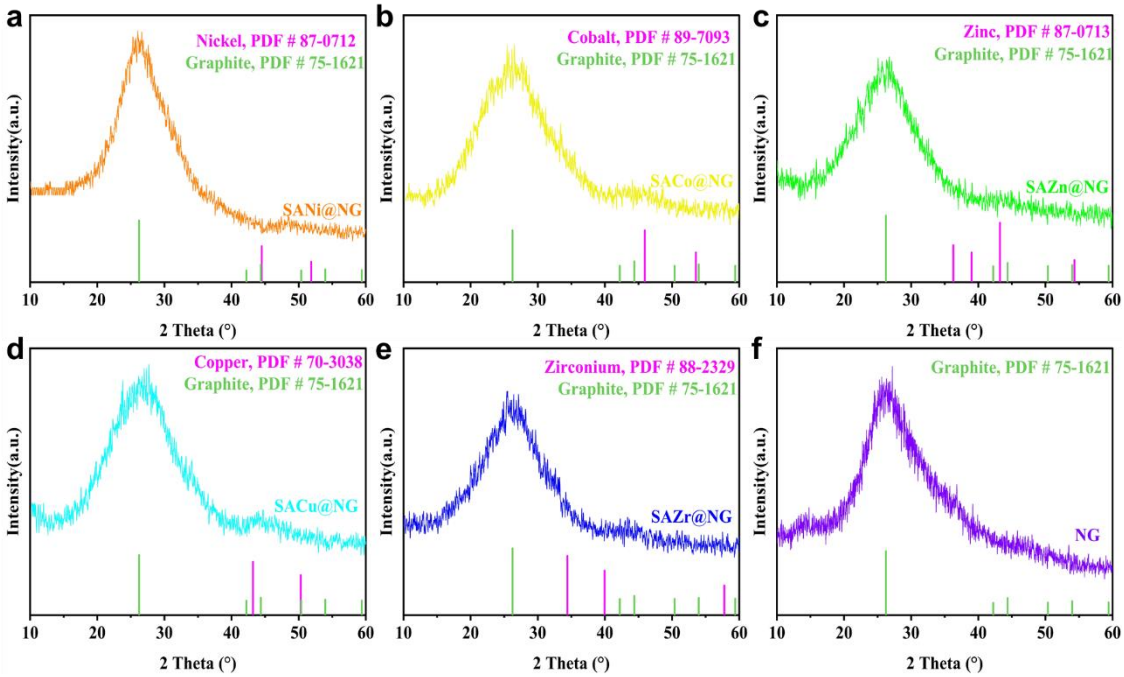

Figure S10. X-ray diffraction (XRD) patterns of the (a) SANi@NG, (b) SACo@NG, (c) SAZn@NG, (d) SACu@NG, (e) SAZr@NG and (f) NG.

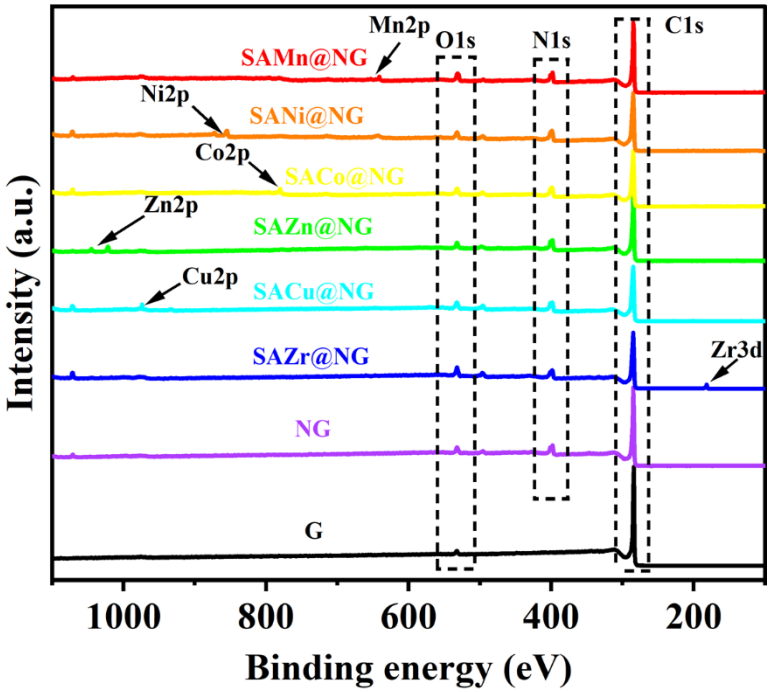

Figure S11. XPS survey spectra of the SAMn@NG (red), SANi@NG (orange), SACo@NG (yellow), SAZn@NG (green), SACu@NG (cyan), SAZr@NG (blue), NG (purple) and G (black).

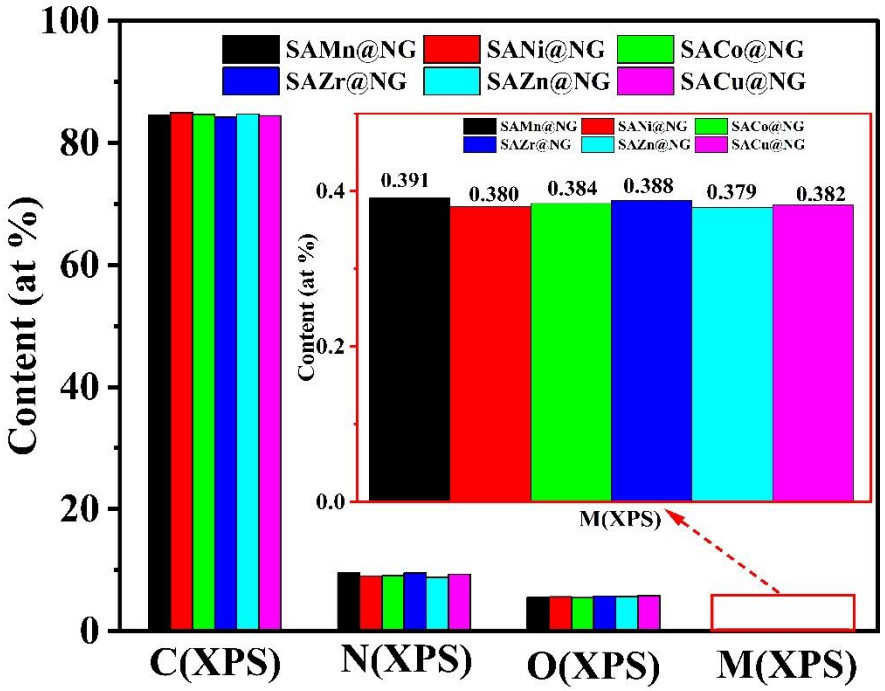

Figure S12. Element content of the SAMn@NG, SANi@NG, SACo@NG, SAZr@NG, SAZn@NG and SACu@NG obtained from XPS measurement (inset shows an enlarged metal atom content).

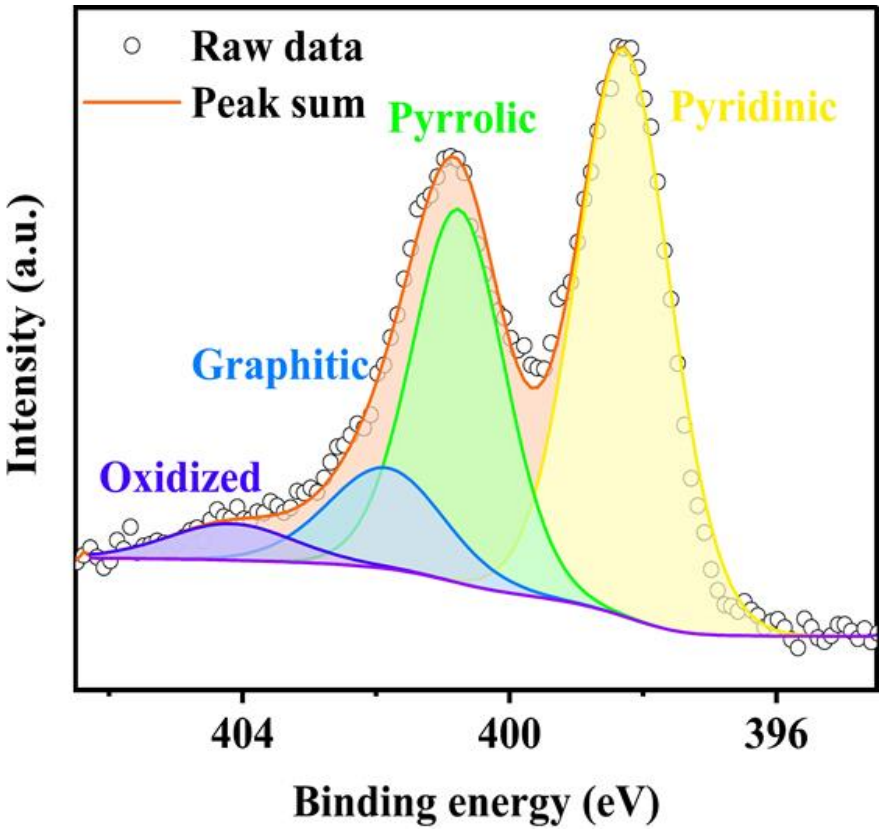

Figure S13. The high-resolution XPS N 1s spectrum of the NG.

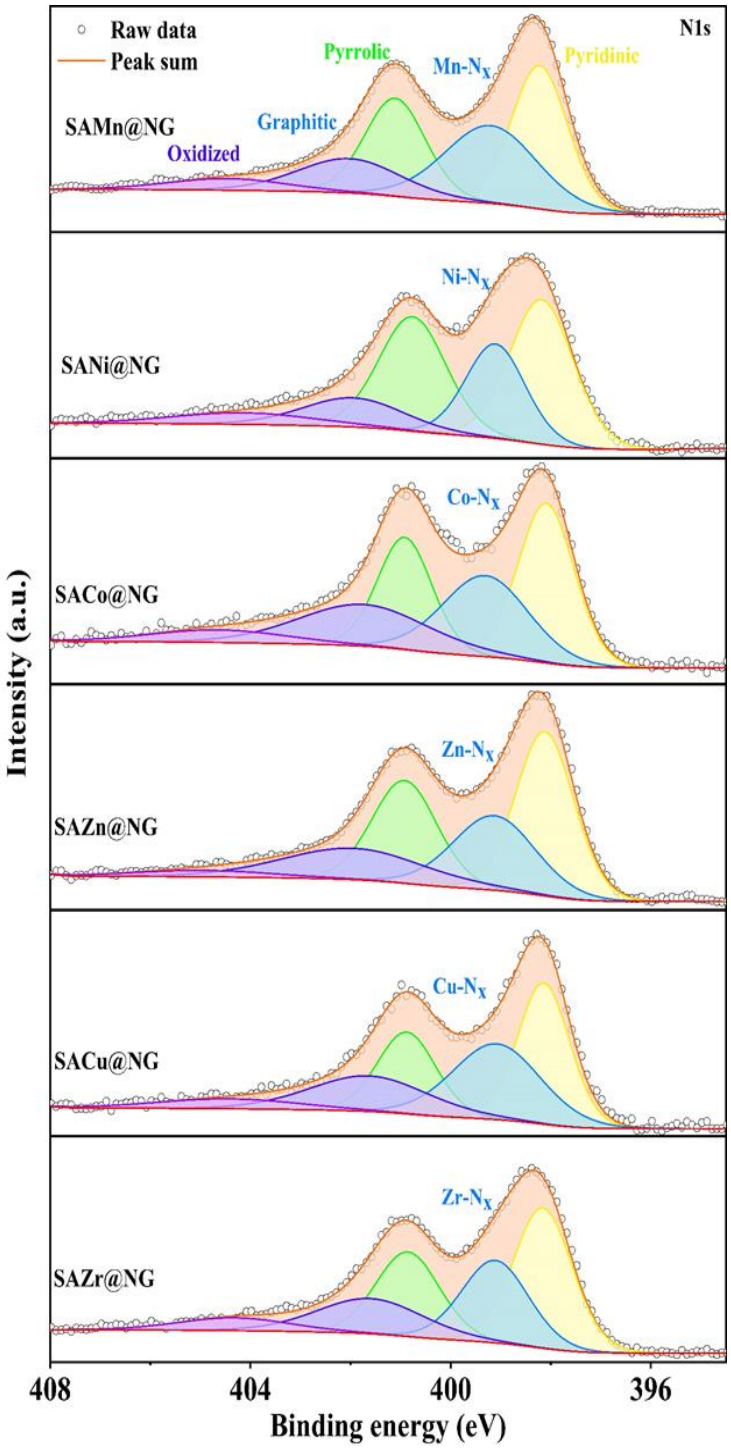

Figure S14. The high-resolution XPS spectrum of N 1s for the SAMn@NG, SANi@NG, SACo@NG, SAZn@NG, SACu@NG and SAZr@NG from top to bottom, respectively.

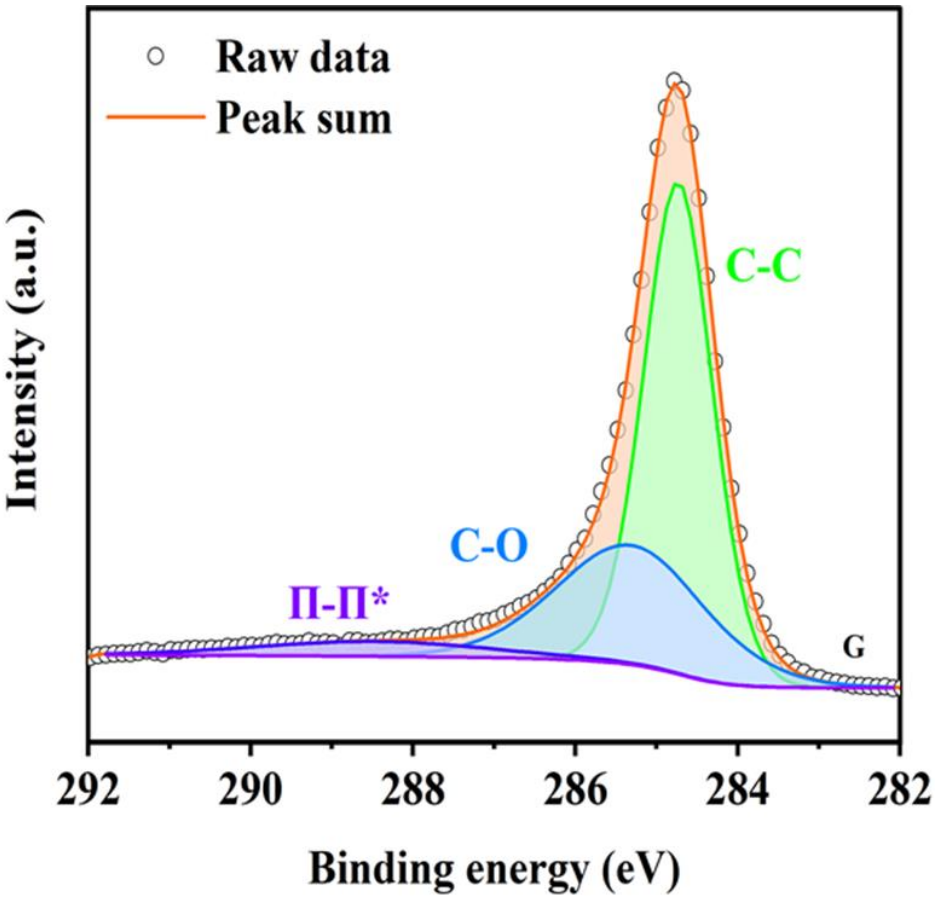

Figure S15. The high-resolution XPS C 1s spectrum of the G.

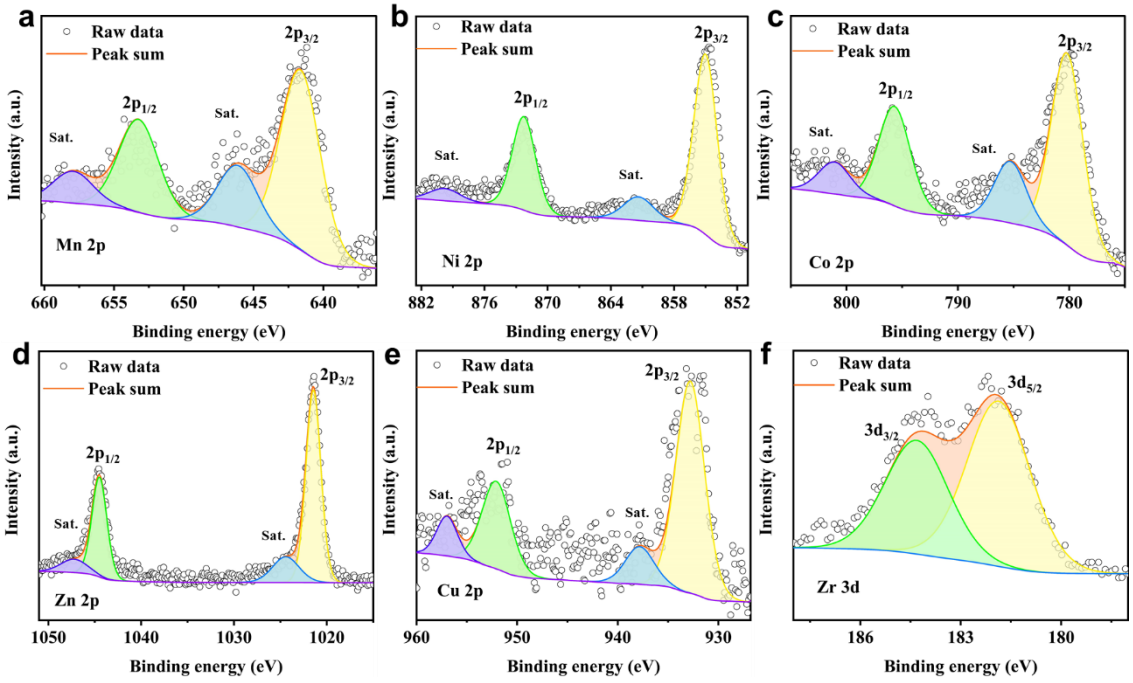

Figure S16. The high-resolution XPS spectrum of (a) Mn 2p, (b) Ni 2p, (c) Co 2p, (d) Zn 2p, (e) Cu 2p and (f) Zr 3d.

The high-resolution XPS spectrum of Mn 2p is shown in **Figure S16a**, at the binding energy of 641.6 eV and 653.2 eV corresponds to Mn $2p_{3/2}$ and Mn $2p_{1/2}$. Two shake-up satellite peaks were observed at 646.0 eV and 657.5 eV. The binding energy of Mn $2p_{3/2}$ (641.6 eV) of SAMn@NG is approximately 0.1 eV lower than that of Mn^{2+} (641.7 eV) and 0.6 eV higher than that of Mn^{0} (641.0 eV), indicating that the valence state of Mn is around +2. In addition, the presence of a specific shaking satellite peak at 646.0 eV also proves this result. [12] As shown in **Figure S16b**, there are four peaks at 854.7 eV (Ni $2p_{3/2}$), 872.3 eV (Ni $2p_{1/2}$), 861.4 eV (satellite peak) and 879.78 eV (satellite peak). The Ni $2p_{3/2}$ of SANi@NG is approximately lower than that of Ni^{2+} (856.0 eV) and higher than that of Ni^{0} (853.5 eV), meaning that the existence form of Ni are likely to be in a low-valent state. [13] **Figure S16c** shows that the Co $2p_{3/2}$ (780.16 eV) of SACo@NG is between Co^{3+} (780.0 eV) and Co^{2+}

(780.3 eV). [14] In the XPS spectrum of Zn 2p (**Figure S16d**), the peaks of SAZn@NG at 1022.1 (Zn $2p_{1/2}$) and 1044.9 eV (Zn $2p_{3/2}$) correspond to the +2 state of Zn.[15] The Cu $2p_{3/2}$ peak at 932.9 eV (**Figure S16e**) is situated between Cu^0 (932.4 eV) and Cu^{2+} (934.6 eV), suggesting that the valence state of Cu in SACu@NG is between 0 and +2. [16] The Zr $3d_{3/2}$ (184.3 eV) and Zr $3d_{5/2}$ (181.9 eV) can be observed in **Figure S16f**, the Zr $3d_{5/2}$ of SAZr@NG is between Zr^+ (179.8 eV) and Zr^{4+} (182.2 eV).[17]

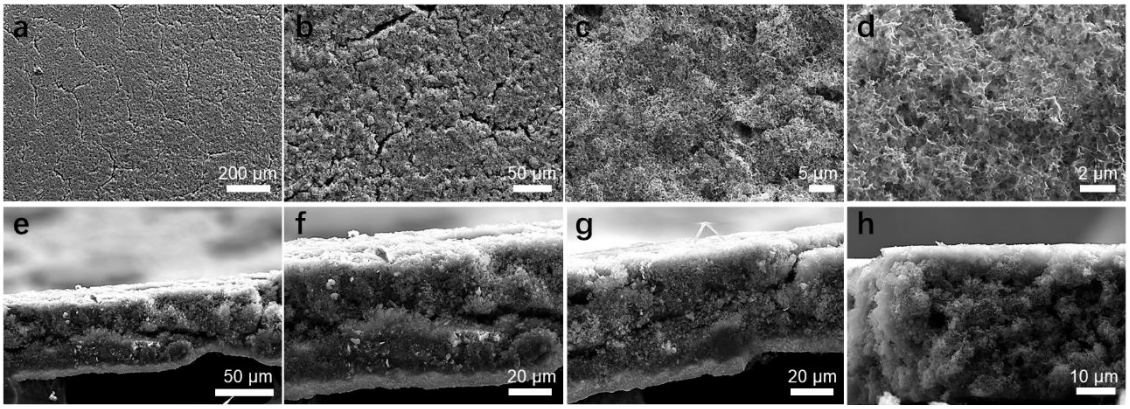

Figure S17. SEM images of Li metal deposited on the SAMn@NG electrodes after plating 3 mAh cm^{-2} at 0.5 mA cm^{-2}. (a–d) cross-section SEM images; (e–h) Top-view SEM images.

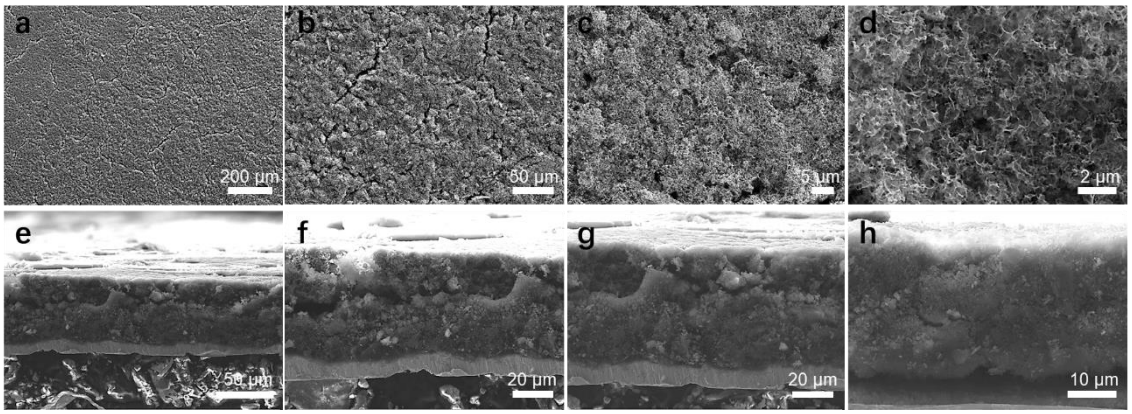

Figure S18. SEM images of Li metal deposited on the SAMn@NG electrodes after plating 5 mAh cm^{-2} at 0.5 mA cm^{-2}. (a–d) cross-section SEM images; (e–h) Top-view SEM images.

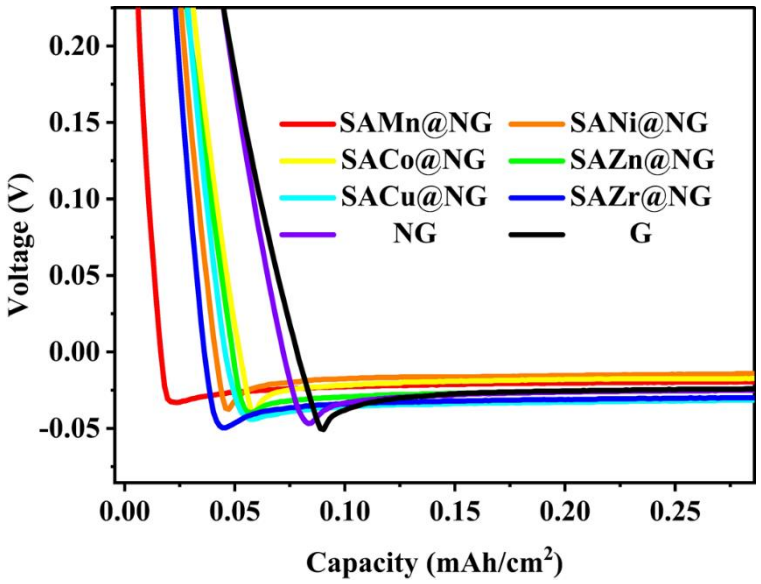

Figure S19. The voltage-areal capacity curves during Li nucleation process at 0.5 mA cm^{-2} on different electrodes. The nucleation overpotential, which is defined as the difference between the bottom of the voltage dip and the later flat part in the voltage profile, is associated with the degree of lithiophilicity of the electrode materials. Obviously, compared with the G electrode, the SA*M*@NG and NG electrodes exhibit a smaller nucleation overpotential.

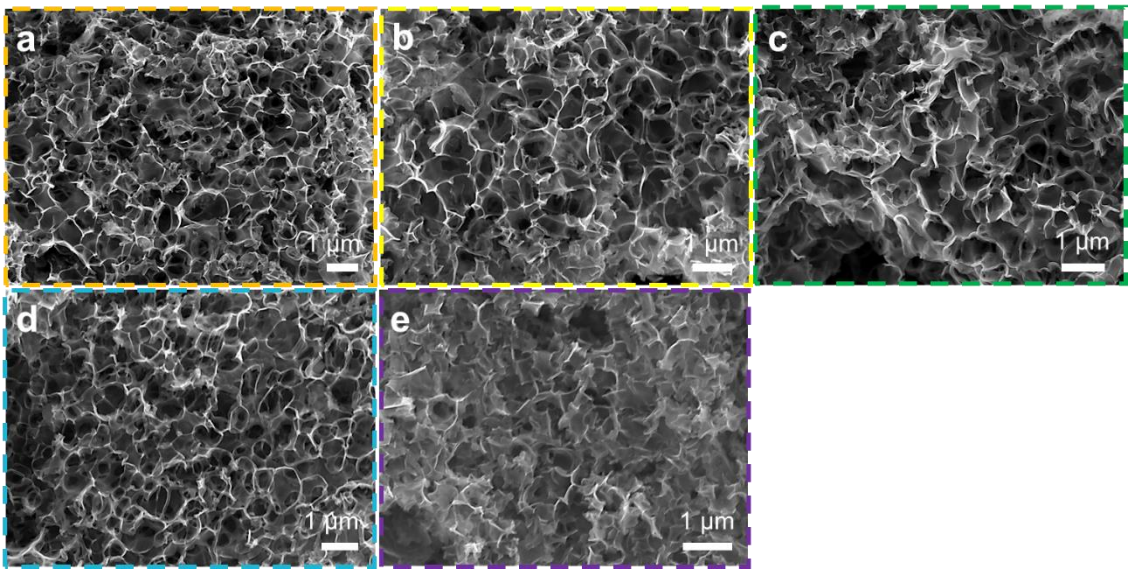

Figure S20. SEM images of the (a) SANi@NG, (b) SACo@NG, (c) SAZn@NG, (d) SACu@NG and (e) NG electrodes after the 100th plating & stripping (testing condition: 1.0 mAh cm^{-2} of Li at 1.0 mA cm^{-2}).

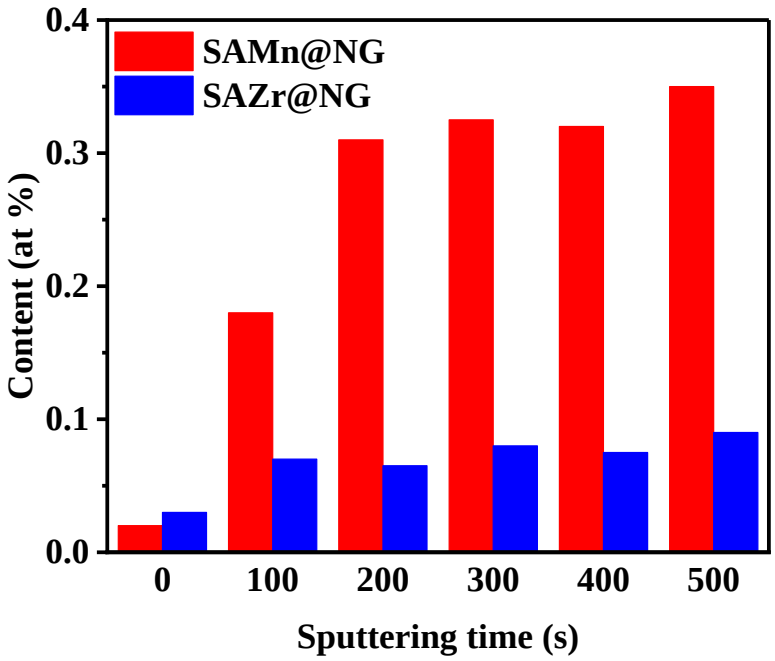

Figure S21. Metal element content of the SAMn@NG and SAZr@NG obtained from XPS depth measurement.

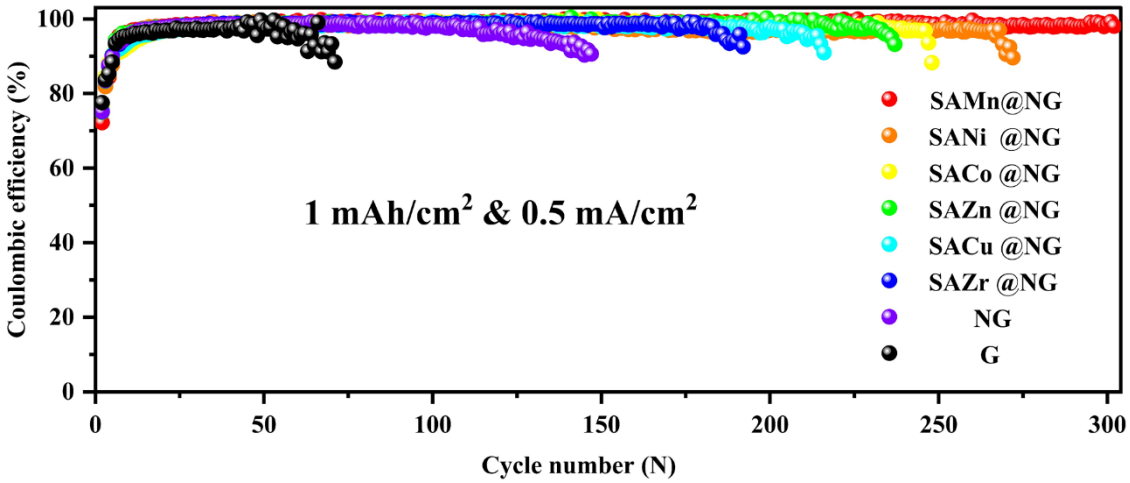

Figure S21. Coulombic efficiency of Li deposition on electrodes (SAMn@NG (red), SANi@NG (orange), SACo@NG (yellow), SAZn@NG (green), SACu@NG (cyan), SAZr@NG (blue), NG (purple) and G (black)) with a capacity of 1 mAh cm^{-2} at 0.5 mA cm^{-2}.

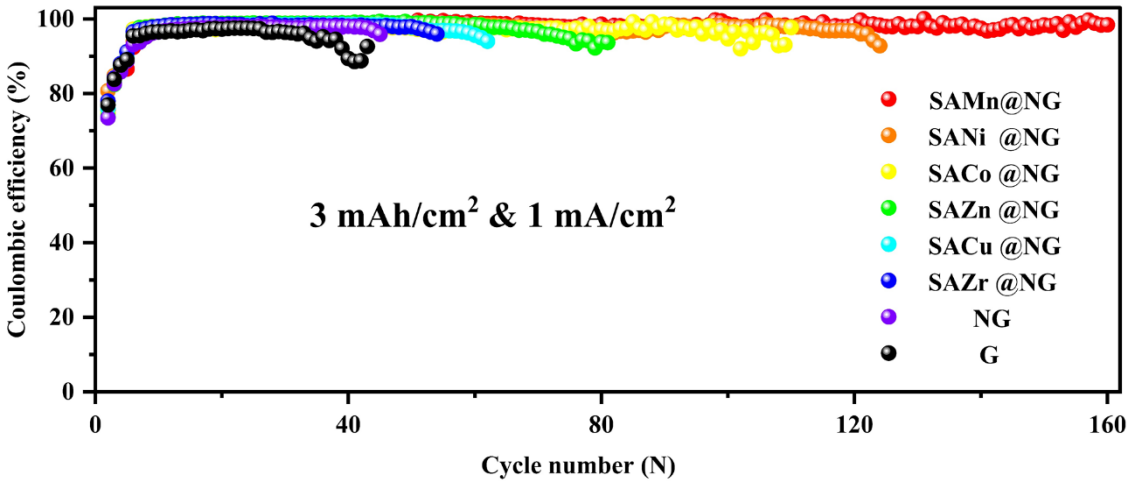

Figure S22. Coulombic efficiency of Li deposition on electrodes (SAMn@NG (red), SANi@NG (orange), SACo@NG (yellow), SAZn@NG (green), SACu@NG (cyan), SAZr@NG (blue), NG (purple) and G (black)) with a capacity of 3 mAh cm^{-2} at 1 mA cm^{-2}.

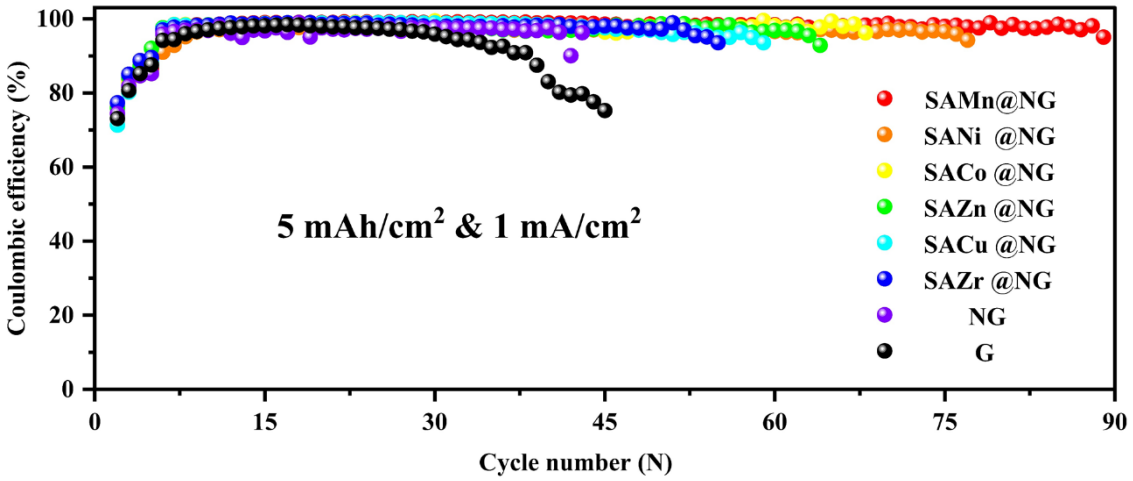

Figure S23. Coulombic efficiency of Li deposition on electrodes (SAMn@NG (red), SANi@NG (orange), SACo@NG (yellow), SAZn@NG (green), SACu@NG (cyan), SAZr@NG (blue), NG (purple) and G (black)) with a capacity of 5 mAh cm^{-2} at 1 mA cm^{-2}.

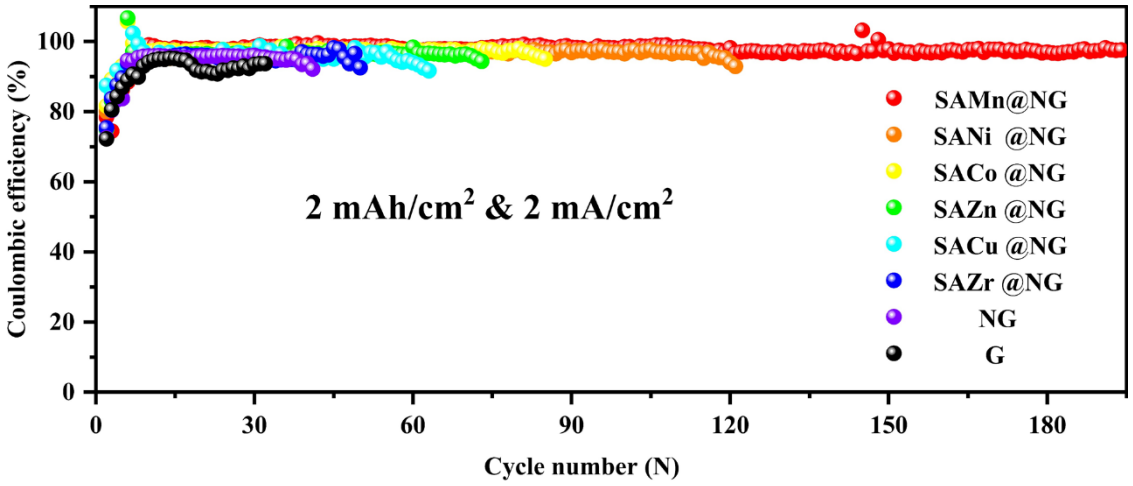

Figure S24. Coulombic efficiency of Li deposition on electrodes (SAMn@NG (red), SANi@NG (orange), SACo@NG (yellow), SAZn@NG (green), SACu@NG (cyan), SAZr@NG (blue), NG (purple) and G (black) with a capacity of 2 mAh cm^{-2} at 2 mA cm^{-2}.

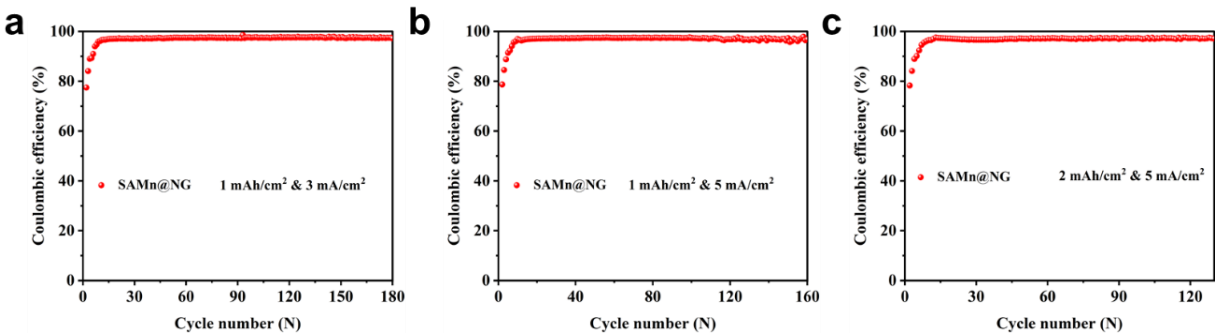

Figure S26. Cycling performances of SAMn@NG electrodes. (a) cycling capacity of 1 mAh cm^{-2} at 3 mA cm^{-2}, (b) cycling capacity of 1 mAh cm^{-2} at 5 mA cm^{-2} and (c) cycling capacity of 2 mAh cm^{-2} at 5 mA cm^{-2}.

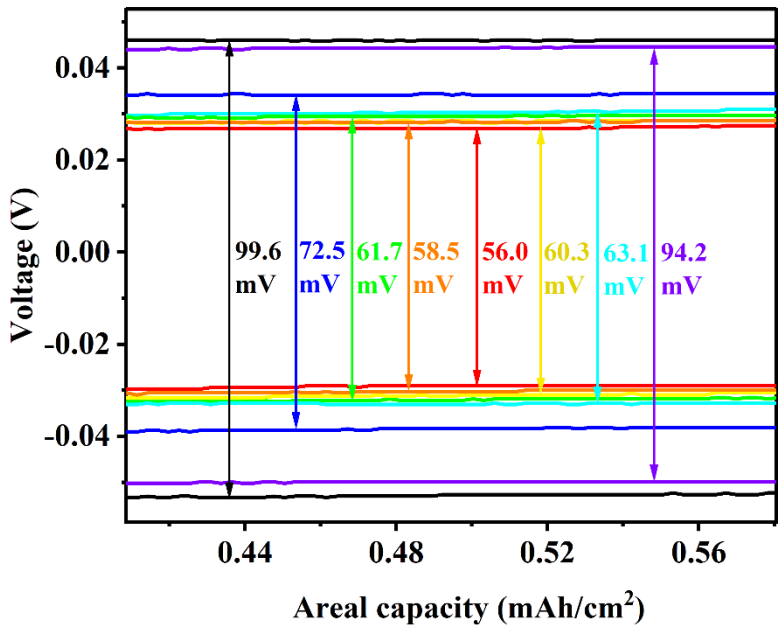

Figure S27. Enlarged view of **Figure 4b** (red frame)

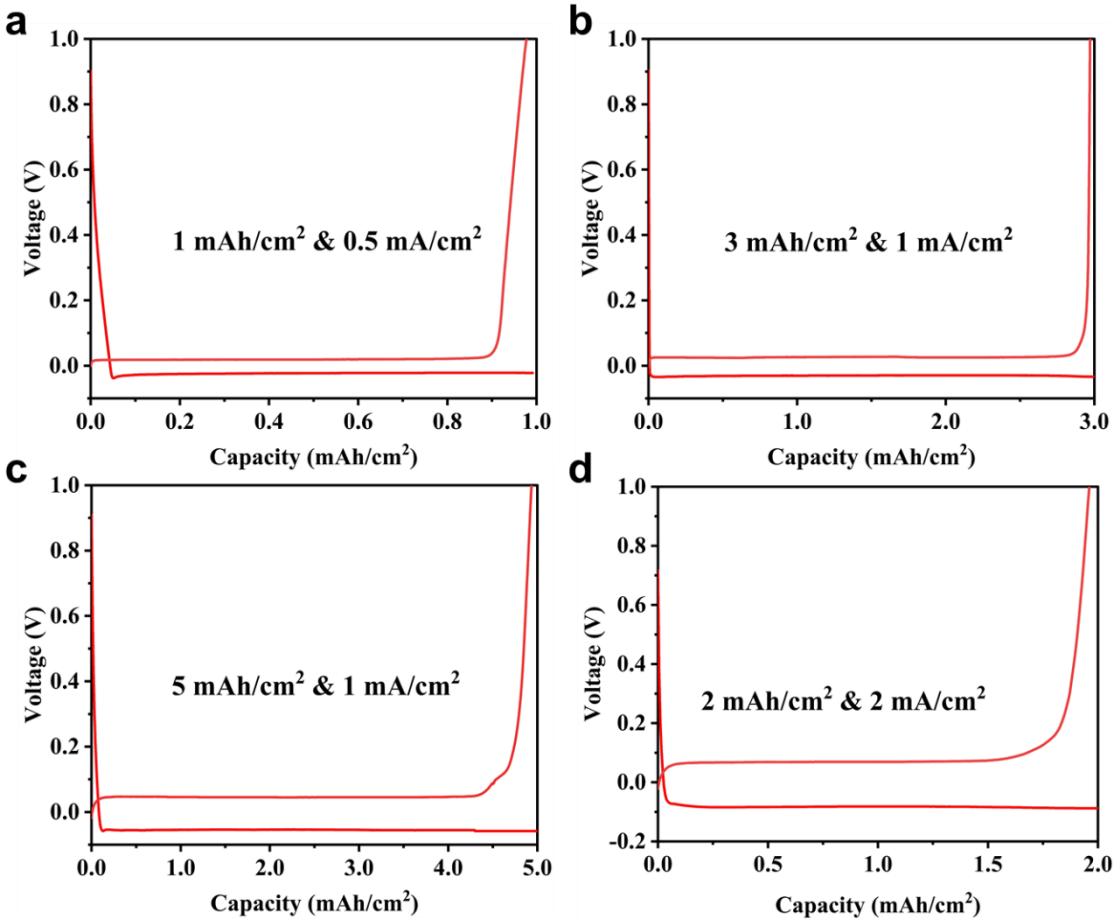

Figure S25. Voltage profiles of SAMn@NG (a) with a capacity of 1 mAh cm^{-2} at 0.5 mA cm^{-2}, (b) with a capacity of 3 mAh cm^{-2} at 1 mA cm^{-2}, (c) with a capacity of 5 mAh cm^{-2} at 1 mA cm^{-2}, (d) with a capacity of 2 mAh cm^{-2} at 2 mA cm^{-2}.

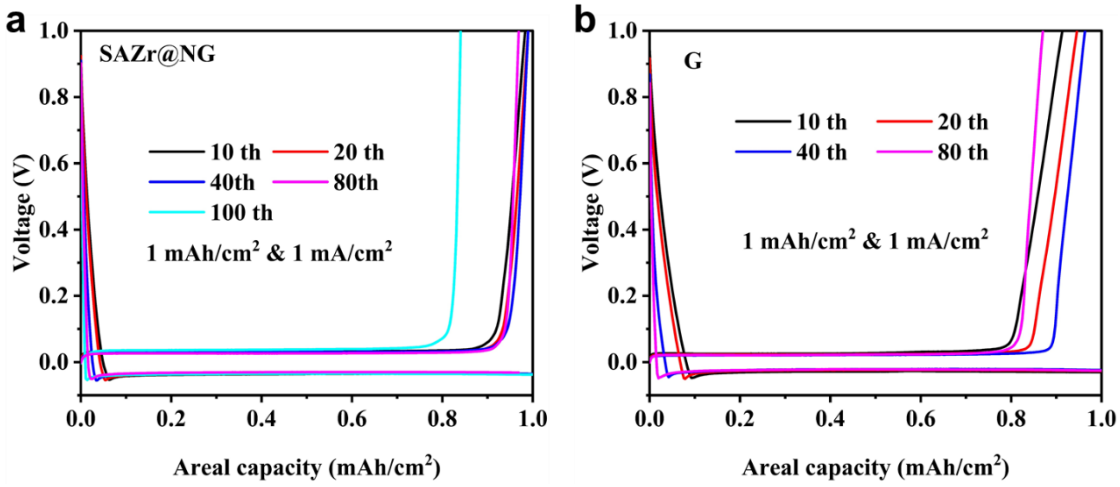

Figure S26. Voltage profiles at different cycles of (a) SAZr@NG and (b) G electrode.

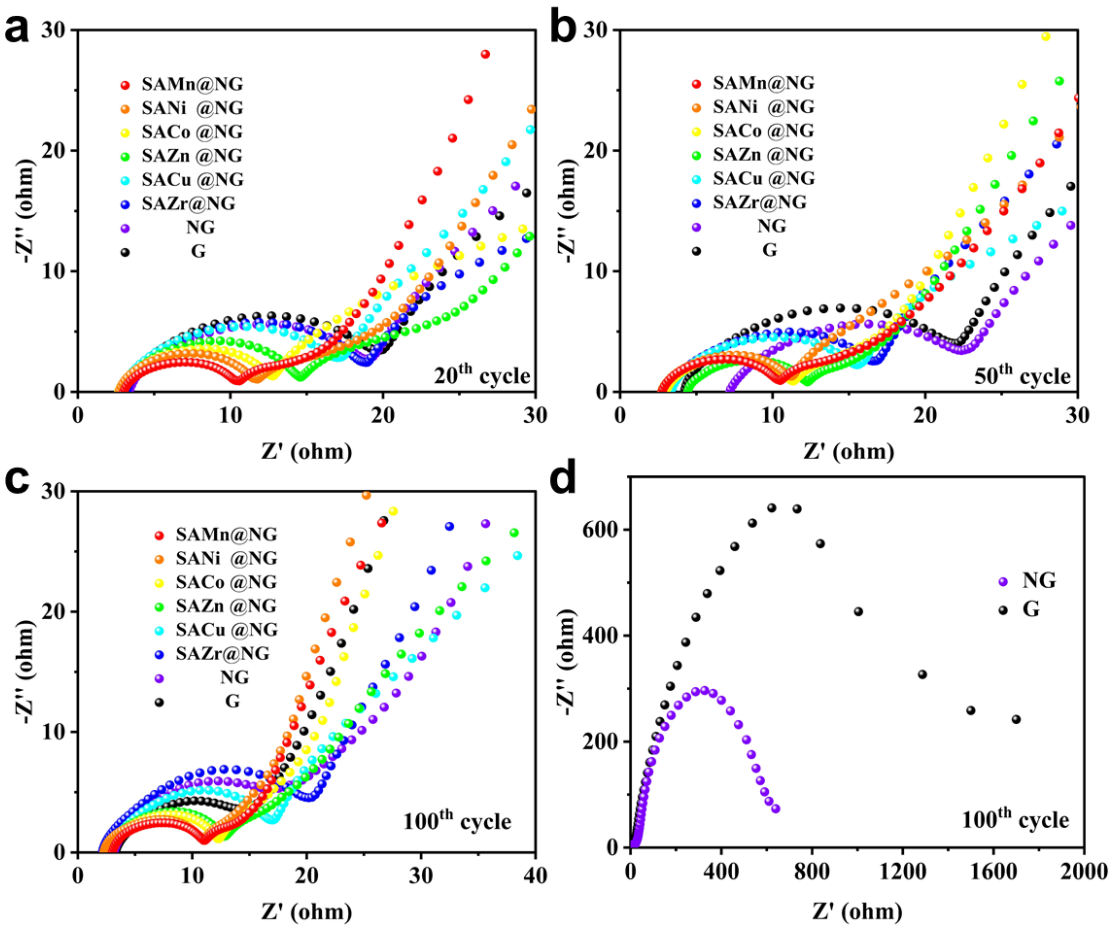

Figure S30. Electrochemical impedance spectroscopy. Nyquist plots of SAMn@NG (red), SANi@NG (orange), SACo@NG (yellow), SAZn@NG (green), SACu@NG (cyan), SAZr@NG (blue), NG (purple) and G (black) electrodes (a) after 20th cycle, (b) after 50th cycle and (c) after 100th cycle. (d) enlarged view of the Nyquist plot of NG and G electrodes after 100th cycle.

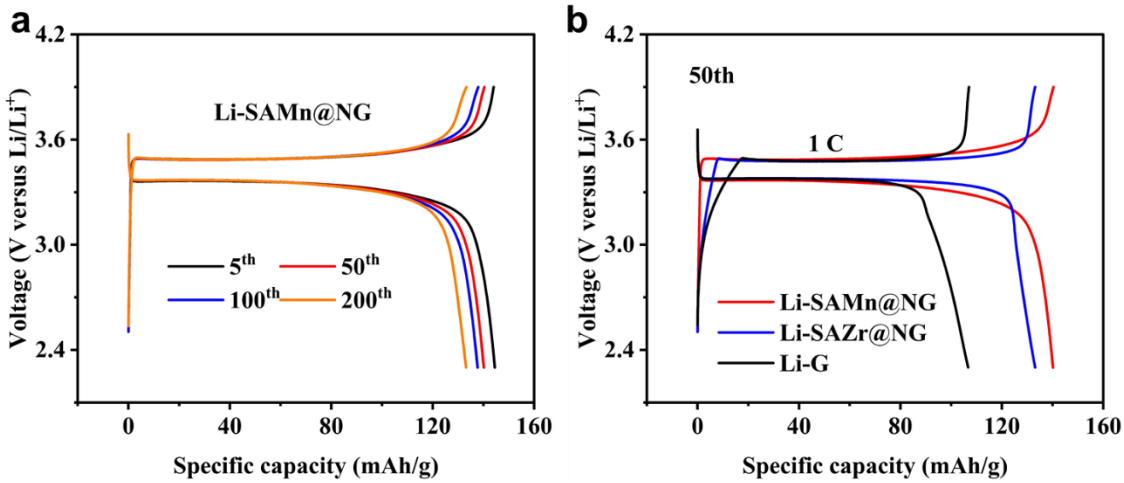

Figure S31. Charge/discharge curves at 1 C of (a) Charge/discharge curves of Li-SAMn@NG||LFP at different cycles and (b) Li-SAMn@NG||LFP (red), Li-SAZr@NG||LFP (blue) and Li-G ||LFP (black) after 50th cycle.

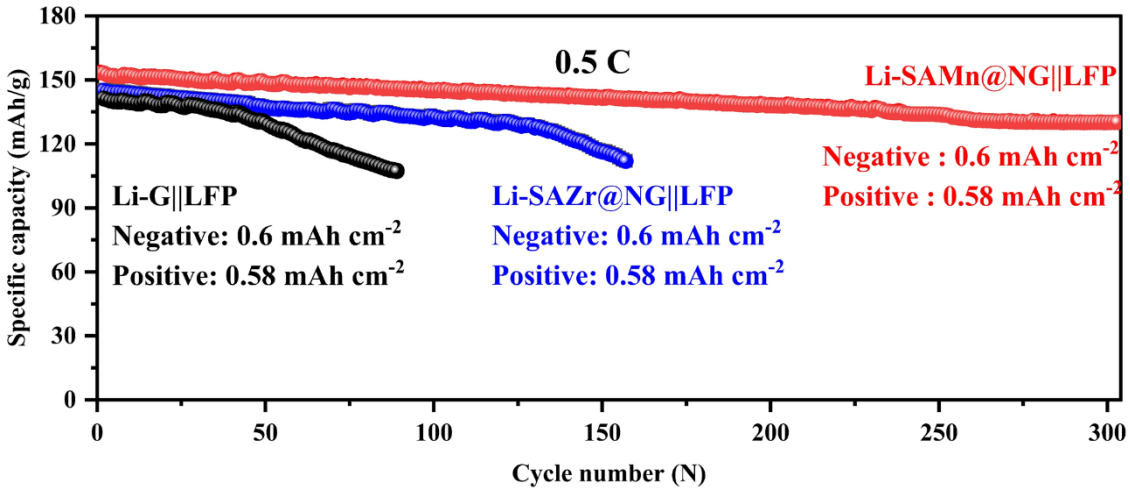

Figure S32. Cycling performances of Li-SAMn@NG||LFP (red), Li-SAZr@NG||LFP (blue) and Li-G||LFP (black) batteries at 0.5 C.

We use the supercell models to simulate the absorption of Li atoms with different concentration (one Li atom in one supercell). The larger the supercell is, the smaller the concentration of Li atoms is. When we decrease the supercell in simulated models, corresponding to increase the concentration of Li atoms.

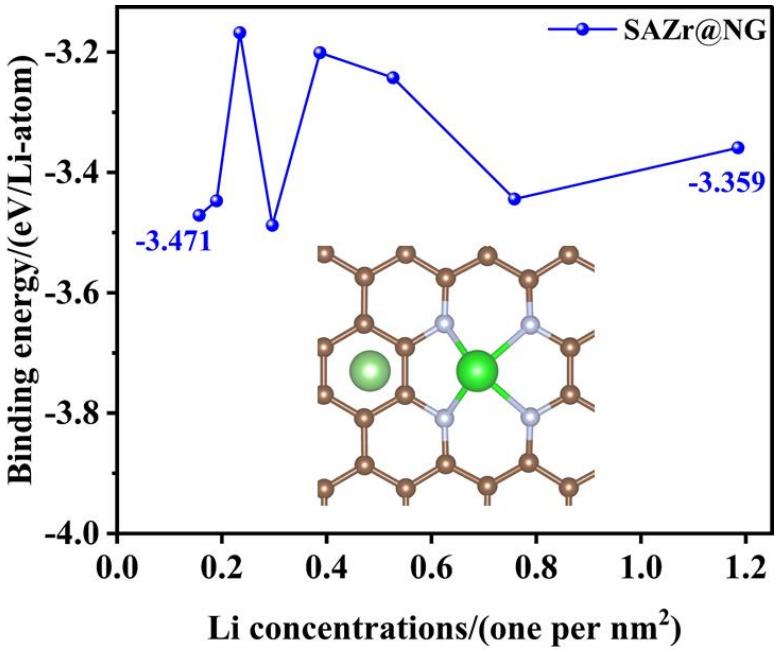

Figure S33. Binding energy (eV/Li-atom) of Li atoms with the change of the concentrations of Li ranging from 0.15 to 1.18 (atoms per square nanometer) on the SAZr@NG. Inset image indicates the Li atomic adsorption configurations for the studied system.

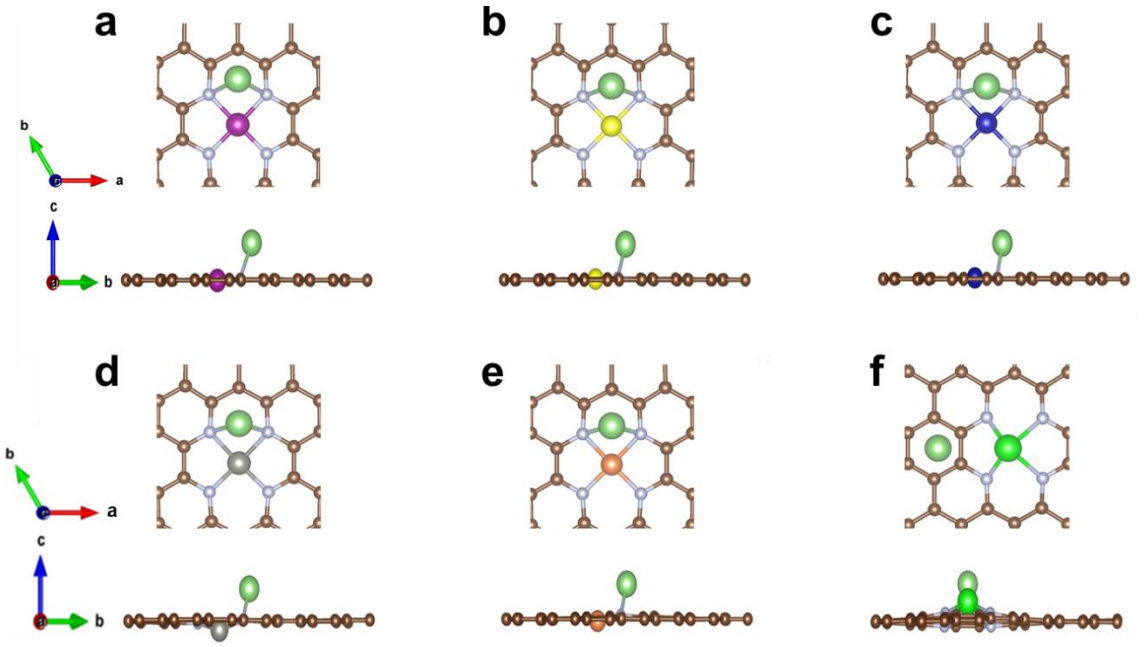

Figure S27. The top view and side view for the most stable adsorption configuration of Li on (a) SAMn@NG, (b) SANi@NG, (c) SACo@NG, (d) SAZn@NG, (e) SACu@NG and (f) SAZr@NG, which was considered to investigate the stability of substrate during the deposition of Li. The lithium, carbon, nitrogen, manganese, nickel, cobalt, zinc, copper, and zirconium are marked with pale green, brown, silver, purple, yellow, dark blue, gray, orange and green, respectively.

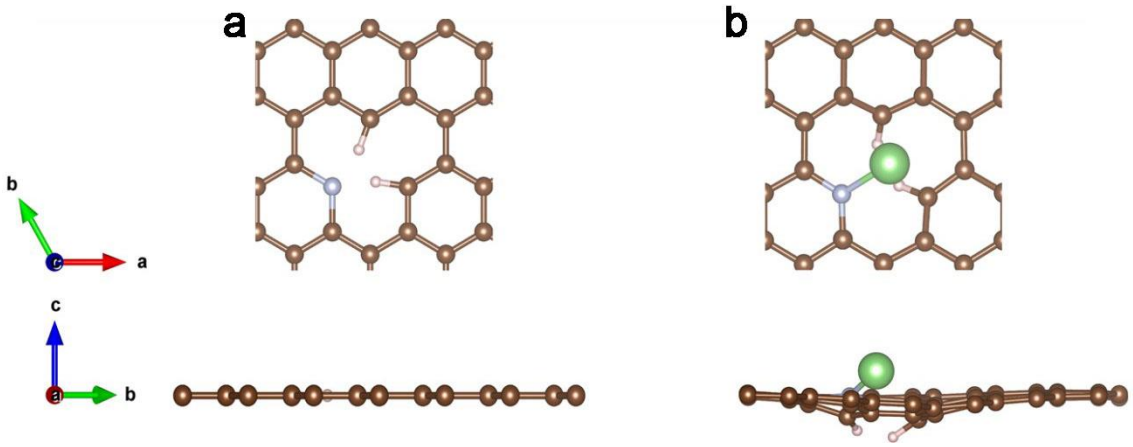

Figure S28. Structural changes of the NG before and after a Li atom adsorption. The top view and side view of NG (a) before adsorption and (b) after adsorption of Li. The lithium, carbon, hydrogen and nitrogen are marked with pale green, brown, pink and silver, respectively.

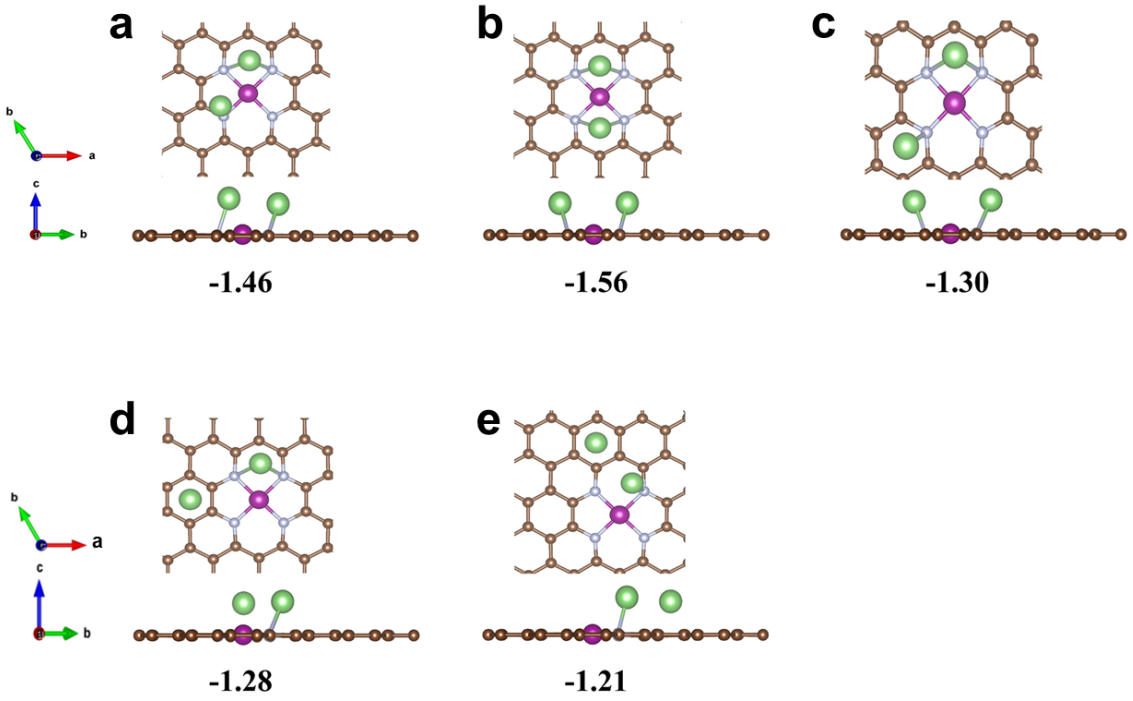

Figure S29. The top view and side view for structure of two Li atoms adsorption on the SAMn@NG. (one Li atom is located at the most stable site during the single atom adsorption, and the other Li atom is all over the possible adsorption sites on the same side) The bottom number is the binding energy (eV/ Li-atom) of Li atom. The lithium, carbon, nitrogen and manganese are marked with pale green, brown, silver and purple, respectively.

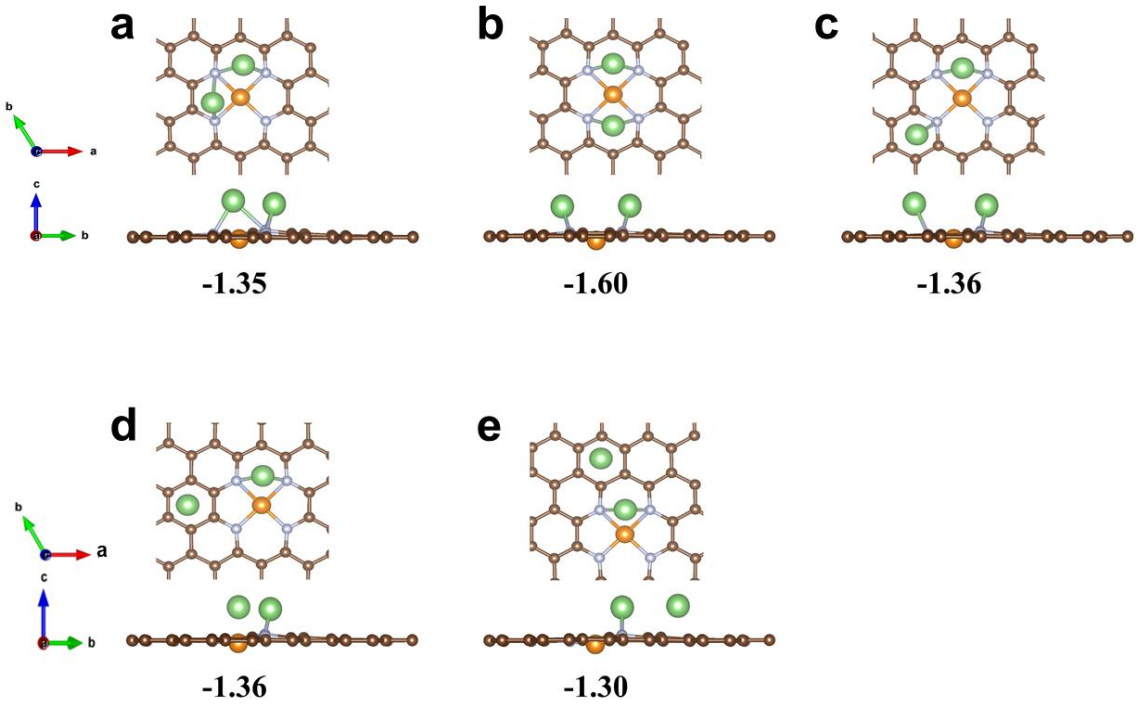

Figure S30. The top view and side view for structure of two Li atoms adsorption on the SACu@NG. (one Li atom is located at the most stable site during the single atom adsorption, and the other Li atom is all over the possible adsorption sites on the same side) The bottom number is the binding energy (eV/ Li-atom) of lithium atom. The lithium, carbon, nitrogen and copper are marked with pale green, brown, silver and orange, respectively.

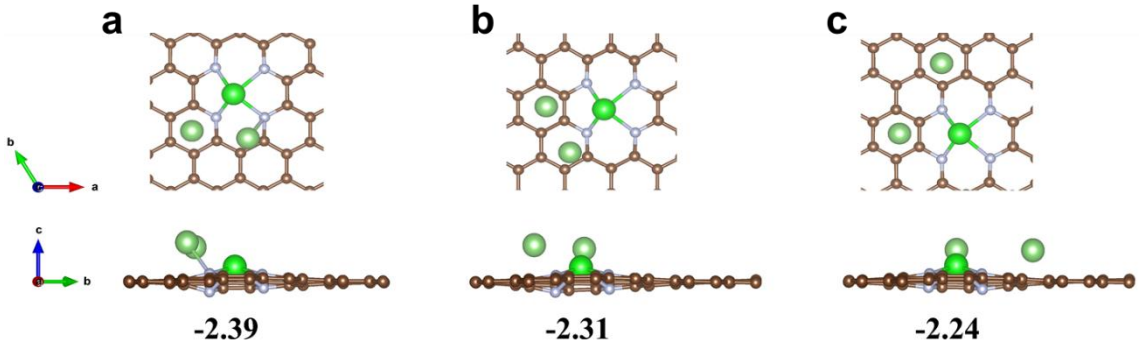

Figure S31. The top view and side view for structure of two Li atoms adsorption on the SAZr@NG. (one Li atom is located at the most stable site during the single atom adsorption, and the other Li atom is all over the possible adsorption sites on the same side) The bottom number is the binding energy (eV/ Li-atom) of lithium atom. The lithium, carbon, nitrogen and zirconium are marked with pale green, brown, silver and green, respectively.

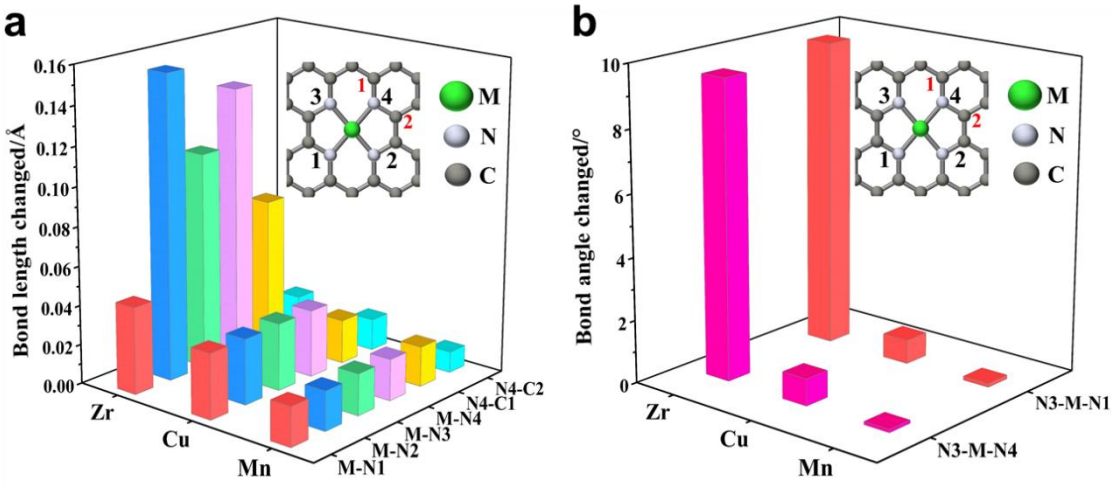

Figure S32. The relative changes of (a) bond lengths and (b) bond angles between metal atoms and the surrounding coordination N atoms before and after the deposition of two Li atoms in the SA*M*@NG (*M*= Mn, Cu, Zr) with labels of illustration showing the corresponding atomic positions.

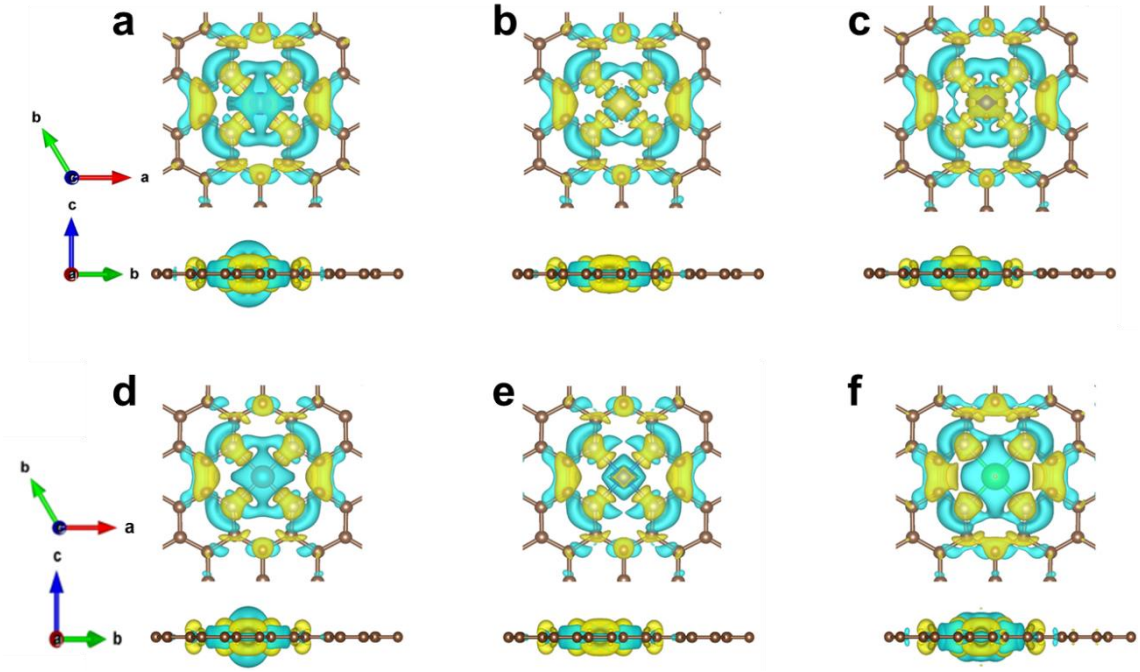

Figure S40. Differential charge density Δρ of the (a) SAMn@NG, (b) SANi@NG, (c) SACo@NG, (d) SAZn@NG, (e) SACu@NG and (f) SAZr@NG, respectively. Δρ is defined as follows, $\Delta\rho=\rho_{slab}-\rho_{no}-\rho_{M}$, where ρ_{slab} is the charge density of the bare SA*M*@NG, ρ_{no} and ρ_{M} are the charge density of SA*M*@NG sheet of the metal atoms being gouged away and single metal atom at the same position as the original SA*M*@NG system, respectively. The yellow and light blue surfaces correspond to the charge gain and lost regions, respectively. The isovalue is 0.002 e $Å^{-3}$.

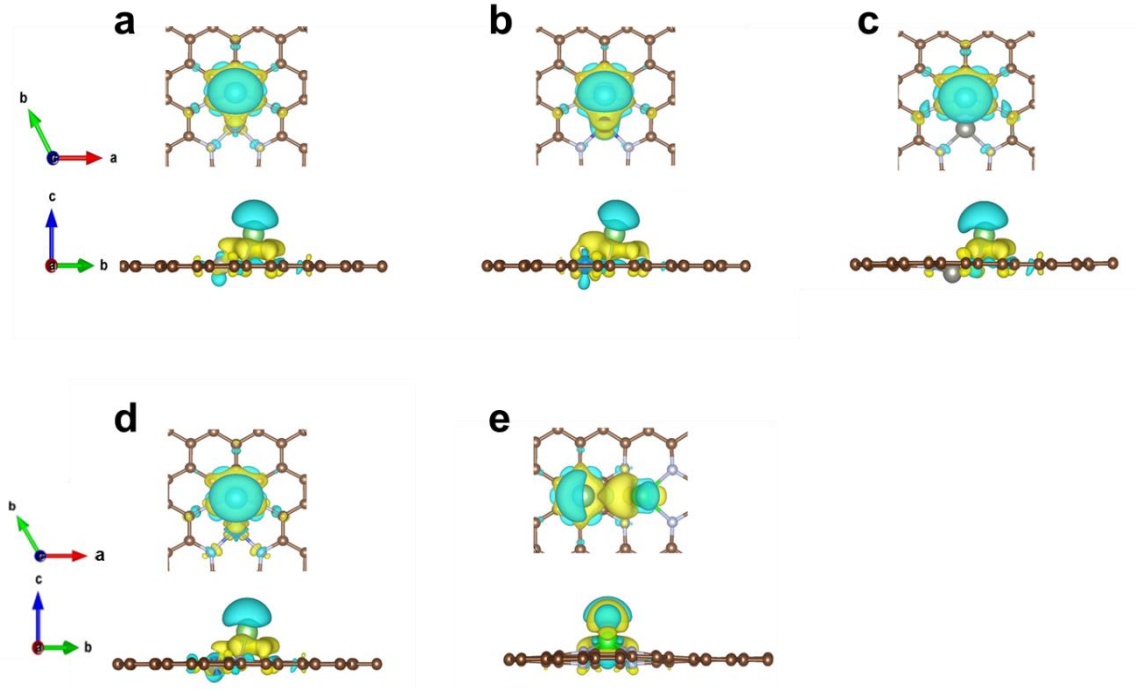

Figure S41. Differential charge density Δρ of the most stable adsorption configuration of a Li atom on (a) SANi@NG, (b) SACo@NG, (c) SAZn@NG, (d) SACu@NG and (e) SAZr@NG, respectively. Δρ is defined as follows, $\Delta\rho=\rho_{total}-\rho_{slab}-\rho_{Li}$, where ρ_{total} is the charge density of the Li adsorbed SA*M*@NG, ρ_{slab} and ρ_{Li} are the charge density of the isolated SA*M*@NG sheet and single Li atom at the same position as the Li-adsorbed SA*M*@NG system, respectively. The yellow and light blue surfaces correspond to the charge gain and lost regions, respectively. The isovalue is 0.002 e $Å^{-3}$.

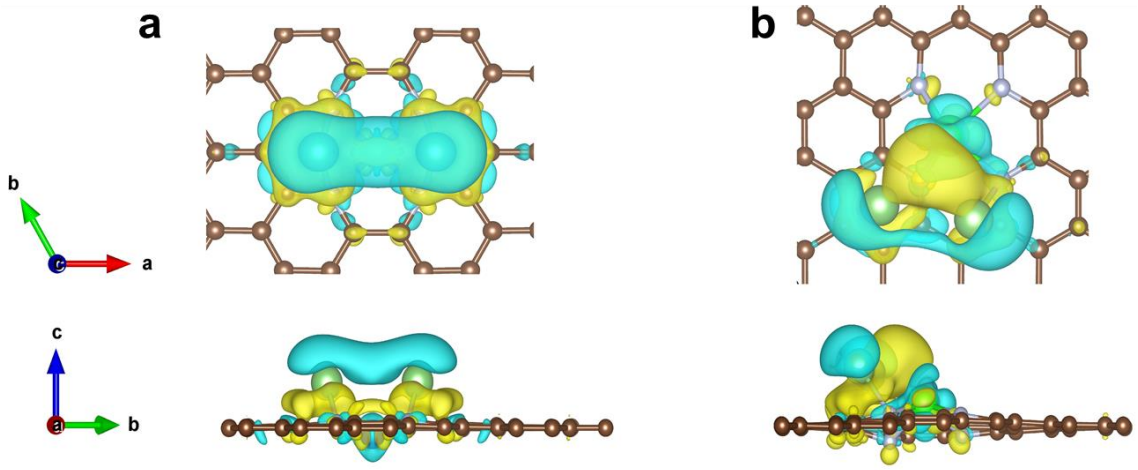

Figure S42. Differential charge density Δρ of the most stable adsorption configuration of two Li atoms on (a) SACu@NG and (b) SAZr@NG. Δρ is defined as follows, $\Delta\rho=\rho_{total}-\rho_{slab}-\rho_{Li}$, where ρ_{total} is the charge density of the Li adsorbed SA*M*@NG, ρ_{slab} and ρ_{Li} are the charge density of the isolated SA*M*@NG sheet and two Li atoms at the same position as the Li-adsorbed SA*M*@NG system, respectively. The yellow and light blue surfaces correspond to the charge gain and lost regions, respectively. The isovalue is 0.002 e $Å^{-3}$.

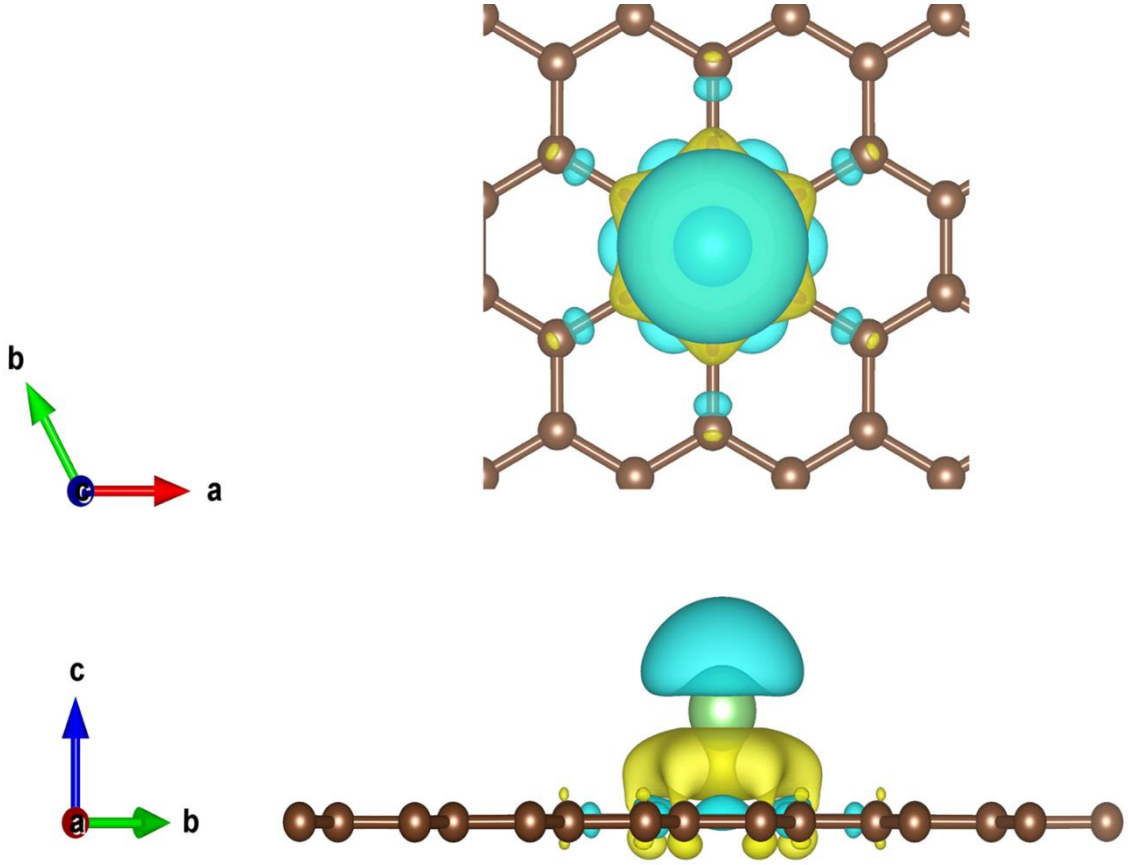

Figure S43. Differential charge density Δρ of a Li atom adsorbed on the Hollow site of Graphene. Δρ is defined as follows, $\Delta\rho=\rho_{total}-\rho_{slab}-\rho_{Li}$, where ρ_{total} is the charge density of the Li adsorbed Graphene, ρ_{slab} and ρ_{Li} are the charge density of the isolated Graphene sheet and single Li atom at the same position as the Li-adsorbed Graphene, respectively. The yellow and light blue surfaces correspond to the charge gain and lost regions, respectively. The isovalue is 0.002 e $Å^{-3}$.

The (111) crystal surface of FCC crystal structure of Au and Ag is adopted, because it has the lowest surface energy compared with other crystal surfaces. The 4×4×1 slab models with five atomic layers are selected, in which two atomic layers on the bottom are fixed to simulate the bulk structure, while the other atomic layers are fully relaxed to find the most stable structures.There are four adsorption sites of Li atoms, namely Top (above the outermost Au/Ag atom) , Bridge (between the two outermost Au/Ag atoms), FCC (above the third layer of Au/Ag atoms from the top down) and HCP (above the second layer of Au/Ag atoms from the top down) site on the surface of Au/Ag metals.

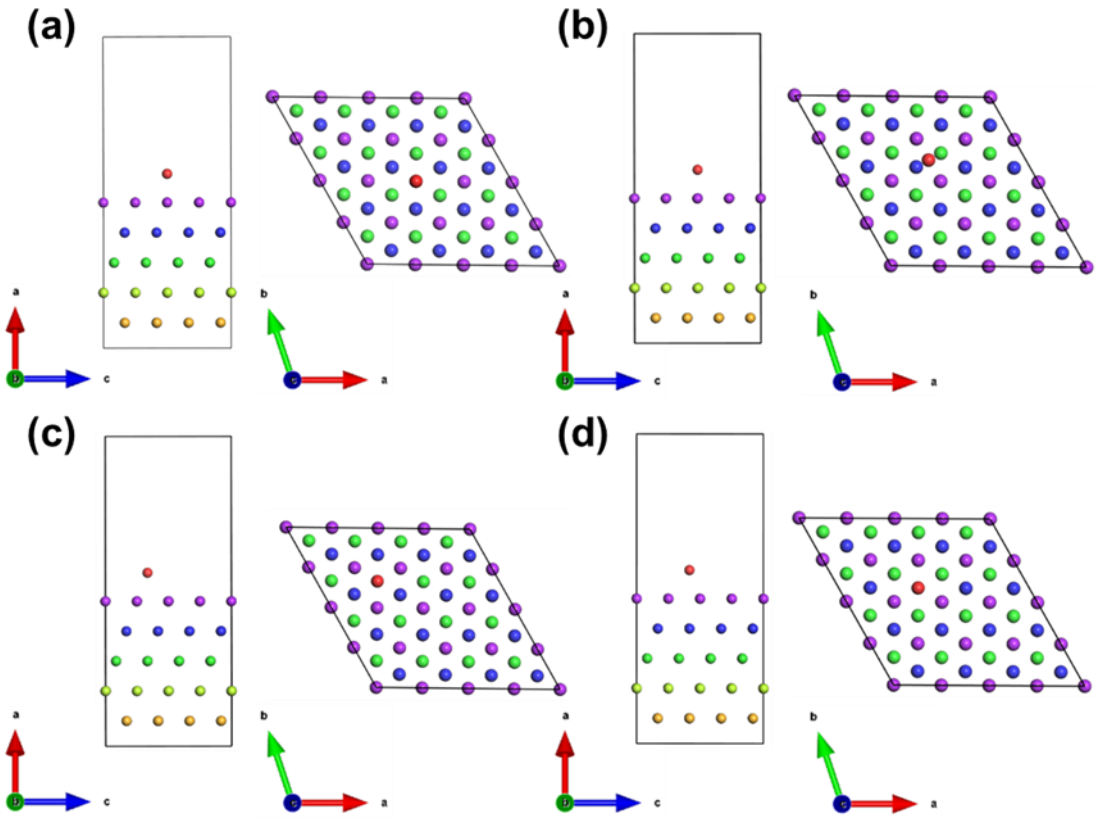

Figure S44. Four configurations for stable adsorption of Li atoms on Au/Ag (111) crystal surface. (a) Top site, (b) Bridge site, (c) FCC (face centered cubic) site and (d) HCP (hexagonal close-packed) site. Li atoms are marked with red, and Ag/Au atoms in the same layer are shown in the same color.

The (221) crystal plane of gray tin (Space group 227, Fd3m) are selected to construct slab model, because (221) crystal surface has the lowest surface energy compared with other crystal surfaces. The 4×1×1 slab models with six atomic layers are selected, in which two atomic layers on the bottom are fixed to simulate the bulk structure, while the other atomic layers are fully relaxed to find the most stable structures. Considering that Li can be deposited on the outermost two layers of Sn atoms, a total of six adsorption configurations are studied.

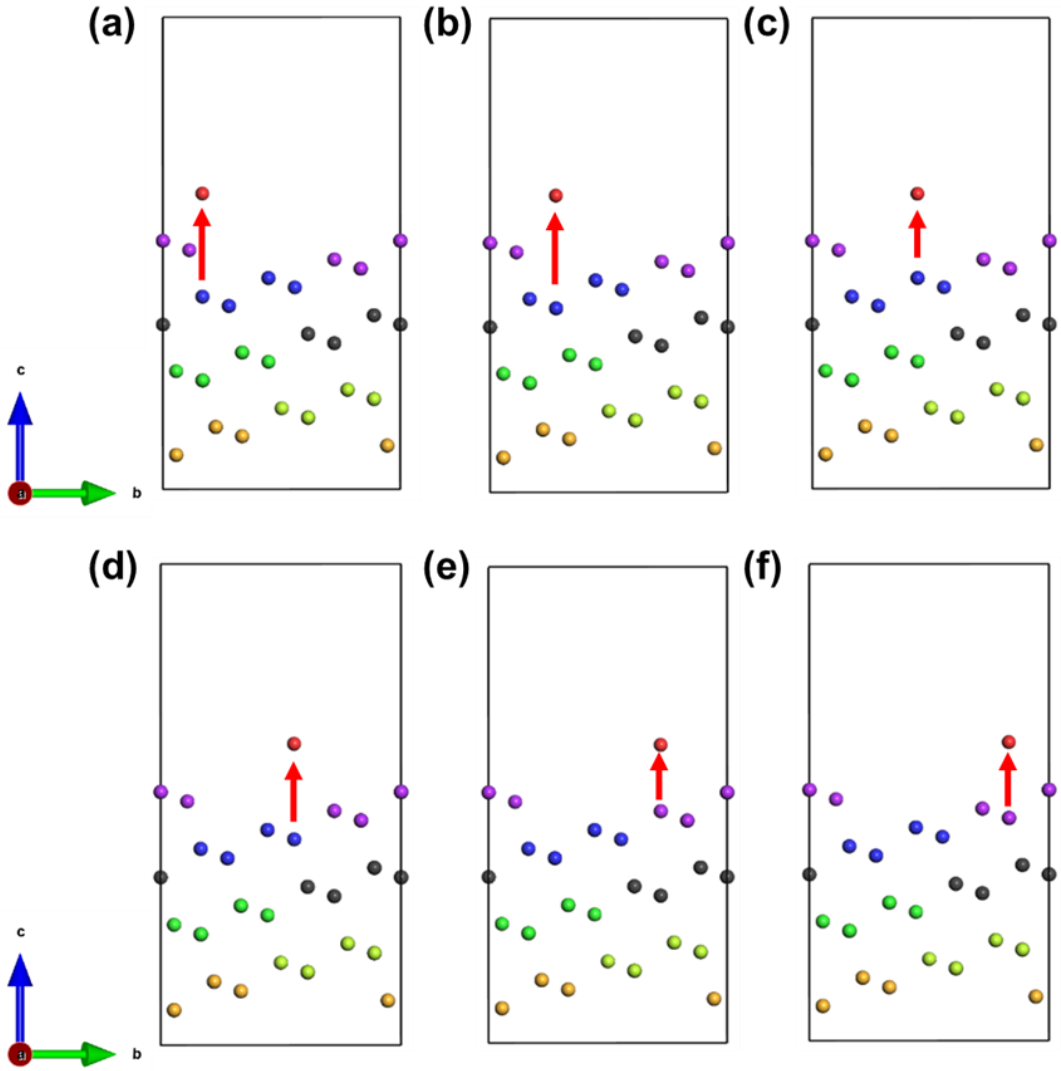

Figure S45. The six adsorption sites of Li atom on the Sn (221) crystal surface, (a) ~(f) correspond to the Top-1 to Top-6 adsorption sites, respectively. The arrow indicates the deposition sites of Li atom above the corresponding Sn atom. Li atoms are marked with red, and Sn atoms in the same layer are shown in the same color.

To quantitatively estimate the amount of charge transfer between the Li adatom and the SA*M*@NG, we have carried out the Bader charge analysis. [18] In this analysis, each atom of a compound is surrounded by a surface (called Bader regions) that runs through minima of the charge density, and the total charge of an atom is determined by integration within the Bader region.

Table S1. The Bader charge state of a Li adatom at the most stable adsorption sites for SAMn@NG, SANi@NG, SACo@NG, SAZn@NG, SACu@NG, SAZr@NG and Graphene, respectively. The slight difference of charge transfer amount may be due to the different coordination environment of the unique metal atom in *M*-N_x-C structure, which leads to the different influence of *M*-N_x-C active site on Li, thus affecting the performance of LMBs.

	SAMn@NG	**SANi@NG**	**SACo@NG**	**SAZn@NG**	**SACu@NG**	**SAZr@NG**	**Graphene**
Bader charge state	+0.90|e|	+0.90|e|	+0.89|e|	+0.81|e|	+0.91|e|	+0.62|e|	0.90|e|

Table S2. The Bader charge state of two Li adatoms at the most stable adsorption sites for SAMn@NG, SACu@NG and SAZr@NG, respectively.

	SAMn@NG	**SACu@NG**	**SAZr@NG**
Bader charge state of two Li adatom	+0.88|e| +0.80|e|	+0.91|e| +0.88|e|	+0.51|e| +0.74|e|

Table S3. The corresponding binding energy of Li atoms on Ag/Au (111) surface.

Adsorption site	Ag (111) Binding Energy/eV	Au (111) Binding Energy/eV
Top	-1.809	-2.506
Bridge	-1.982	-2.650
FCC	-2.005	-2.689
HCP	-2.003	-2.684

Table S4. The corresponding binding energy of Li atoms on Sn (221) surface.

Adsorption site	Sn (221) Binding Energy/eV
Top-1	-2.319
Top-2	-2.388
Top-3	-1.718
Top-4	-2.294
Top-5	-2.322
Top-6	-2.454

References

[1] Kresse, G., Furthmüller, J. J. C. m. s., *Comput. Mater. Sci.* **1996,** *6*, 15.

[2] Kresse, Hafner, *Phys. Rev. B: Condens. Matter Mater. Phys.* **1993,** *48*, 13115.

[3] Momma, K., Izumi, F., *J. Appl. Crystallogr.* **2011,** *44*, 1272.

[4] Momma, K., Izumi, F., *J. Appl. Crystallogr.* **2008,** *41*, 653.

[5] Perdew, J. P., Burke, K., Ernzerhof, M. J. P. r. l., Phys. Rev. Lett. **1996,** *77*, 3865.

[6] Methfessel, Paxton, *Phys. Rev. B: Condens. Matter Mater. Phys.* **1989,** *40*, 3616.

[7] Kresse, G., Joubert, D. J. P. r. b., *Phys. Rev. B: Condens. Matter Mater. Phys.* **1999,** *59*, 1758.

[8] Grimme, S., Ehrlich, S., Goerigk, L., *J. Comput. Chem.* **2011,** *32*, 1456.

[9] Grimme, S., Antony, J., Ehrlich, S., Krieg, H., *J. Chem. Phys.* **2010,** *132*, 154014.

[10] Yang, G., Li, L.; Lee, W. B., Ng, M. C. J. S., materials, t. o. a., Sci. Technol. Adv. Mater. **2018,** *19*, 613.

[11] Monkhorst, H. J., Pack, J. D. J. P. r. B., *Phys. Rev. B: Condens. Matter Mater. Phys.* **1976,** *13*, 5188.

[12] Guo, Z., Xie, Y., Xiao, J., Zhao, Z. J., Wang, Y., Xu, Z., Zhang, Y., Yin, L., Cao, H., Gong, J., *J. Am. Chem. Soc.* **2019,** *141*, 12005.

[13] Yang, H. B., Hung, S.-F., Liu, S., Yuan, K., Miao, S., Zhang, L., Huang, X., Wang, H.-Y., Cai, W., Chen, R., Gao, J., Yang, X., Chen, W., Huang, Y., Chen, H. M., Li, C. M., Zhang, T., Liu, B., *Nat. Energy* **2018,** *3*, 140.

[14] Pan, Y., Lin, R., Chen, Y., Liu, S., Zhu, W., Cao, X., Chen, W., Wu, K., Cheong, W. C., Wang, Y., Zheng, L., Luo, J., Lin, Y., Liu, Y., Liu, C., Li, J., Lu, Q., Chen, X., Wang, D., Peng, Q., Chen, C., Li, Y., *J. Am. Chem. Soc.* **2018,** *140*, 4218.

[15] Han, L.; Song, S.; Liu, M.; Yao, S.; Liang, Z.; Cheng, H.; Ren, Z.; Liu, W.; Lin, R.; Qi, G.; Liu, X.; Wu, Q.; Luo, J.; Xin, H. L., *J. Am. Chem. Soc.* **2020,** *142*, 12563.

[16] Qu, Y. T., Li, Z. J., Chen, W. X., Lin, Y., Yuan, T. W., Yang, Z. K., Zhao, C. M., Wang, J., Zhao, C., Wang, X., Zhou, F. Y., Zhuang, Z. B., Wu, Y., Li, Y. D., *Nat. Catal.* **2018,** *1*, 781.

[17] Mizuno, N., Fujii, H., Igarashi, H., Misono, M. J. J. o. t. A. C. S., *J. Am. Chem. Soc.* **1992,** *114*, 7151.

[18] Henkelman, G., Arnaldsson, A., Jónsson, H. J. C. M. S., Comput. Mater. Sci. **2006,** *36*, 354.